

CHEMICAL COMPOSITIONS OF EVOLVED STARS FROM NEAR-INFRARED IGRINS HIGH-RESOLUTION SPECTRA. I. ABUNDANCES IN THREE RED HORIZONTAL BRANCH STARS

MELIKE AFŞAR^{1,2}, CHRISTOPHER SNEDEN², MICHAEL P. WOOD³, JAMES E. LAWLER⁴, ZEYNEP BOZKURT¹, GAMZE BÖCEK TOPCU¹, GREGORY N. MACE², HWIHYUN KIM⁵, AND DANIEL T. JAFFE²

¹Department of Astronomy and Space Sciences, Ege University, 35100 Bornova, İzmir, Turkey; melike.afsar@ege.edu.tr, zeynep.bozkurt@ege.edu.tr, gamzebocek@gmail.com

²Department of Astronomy and McDonald Observatory, The University of Texas, Austin, TX 78712, USA; afsar@astro.as.utexas.edu, chris@verdi.as.utexas.edu

³Department of Physics, University of St. Thomas, 2115 Summit Ave, St. Paul, Minnesota 55104; mpwood@stthomas.edu

⁴Department of Physics, University of Wisconsin-Madison, 1150 University Ave, Madison, WI 53706; jelawler@wisc.edu

⁵Gemini Observatory, Casilla 603, La Serena, Chile

ABSTRACT

We have derived elemental abundances of three field red horizontal branch stars using high-resolution ($R \simeq 45,000$), high signal-to-noise ratio ($S/N \gtrsim 200$) H and K band spectra obtained with the Immersion Grating Infrared Spectrograph (IGRINS). We have determined the abundances of 21 elements including α (Mg, Si, Ca, S), odd-Z (Na, Al, P, K), Fe-group (Sc, Ti, Cr, Co, Ni), neutron-capture (Ce, Nd, Yb), and CNO group elements. S, P and K are determined for the first time in these stars. H and K band spectra provide a substantial number of S I lines, which potentially can lead to a more robust exploration of the role of sulfur in the cosmochemical evolution of the Galaxy. We have also derived $^{12}\text{C}/^{13}\text{C}$ ratios from synthetic spectra of the first overtone (2–0) and (3–1) ^{12}CO and (2–0) ^{13}CO lines near 23440 Å and ^{13}CO (3–1) lines at about 23730 Å. Comparison of our results with the ones obtained from the optical region suggests that the IGRINS high-resolution H and K band spectra offer more internally self-consistent atomic lines of the same species for several elements, especially the α elements. This in turn provides more reliable abundances for the elements with analytical difficulties in the optical spectral range.

Keywords: stars: abundances – stars: atmospheres – stars: evolution – stars: horizontal-branch – stars: individual (HIP 54048, HIP 57748, HIP 114809) – instrumentation: spectrographs

1. INTRODUCTION

Low mass core helium burning stars appear in the HR diagram as members of the horizontal branch (HB). These highly evolved objects have effective temperatures that span $4800 \text{ K} \lesssim T_{\text{eff}} \lesssim 25,000 \text{ K}$ and absolute magnitudes with only a small range, $0 \sim M_V \sim +1$. HB stars are subdivided into four temperature groups: red clump and red horizontal branch (RC and RHB, $\sim 4800\text{--}6000 \text{ K}$), the RR Lyrae instability strip ($\sim 6000\text{--}7500 \text{ K}$), blue (BHB, $\sim 7500\text{--}20,000 \text{ K}$), and extreme (EBHB ($\gtrsim 25,000 \text{ K}$)). As discussed in Afşar et al. 2018a (hereafter Afşar18a), RHB stars are low mass core-helium-burning stars. Afşar18a follows the observational RHB definition given by Kaempf et al. (2005) and defines an RHB range for the stars around solar metallicity with $0.5 \lesssim (B-V) \lesssim 1.0$ and $-0.5 \lesssim M_V \lesssim 1.5$. This “box” also includes so called “secondary red clump” defined by, e.g., Girardi et al. (1998) and Girardi (1999), in which they investigate secondary clump for different metallicities in synthetic color-magnitude diagrams (e.g. Figure 7 in Girardi 1999). HB astrophysical interests are many, from distance indicators, to stellar population studies, to signposts for interior advanced nucleosynthesis and envelope mixing.

HB stars with Galactic disk metallicities ($[\text{Fe}/\text{H}] \gtrsim -1$)¹, e.g., metal-rich globular clusters and field thick disk stars, almost always occupy the RHB². In these older populations there is no evolutionary state ambiguity, since subgiant stars in the RHB temperature domain have much lower luminosities, $M_V \gtrsim +3.5$. However in the general Galactic field the low mass thick disk He-burning stars can share the same ($T_{\text{eff}}, \log g$) or ($B-V, M_V$) domain with higher-mass thin

¹ We adopt the standard spectroscopic notation (Wallerstein & Helfer 1959) that for elements A and B, $[A/B] \equiv \log_{10}(N_A/N_B)_* - \log_{10}(N_A/N_B)_\odot$. We use the definition $\log \epsilon(A) \equiv \log_{10}(N_A/N_H) + 12.0$, and equate metallicity with the stellar $[\text{Fe}/\text{H}]$ value.

² Metal-rich globular clusters with BHB stars are rare; notable exceptions are the metal-rich globular clusters NGC 6388 and NGC 6441 ($[\text{Fe}/\text{H}] \simeq -0.6$) that have both prominent RHB and BHB populations (Rich et al. 1997).

disk subgiants, and also can be confused with the occasional thin-disk He core-burning stars near the high-mass edge of the metal-rich red giant “clump”. These stellar population confusions, combined with difficulties in determining accurate distances, have hampered the identification of field stars likely to be true RHB stars, thus rendering them under-studied compared to red giants.

Kaempf et al. (2005) conducted a large-scale photometric survey of field stars with Hipparcos parallaxes (van Leeuwen 2007), and proposed a $(B - V, M_V)$ area likely to be dominated by RHB stars. Early spectroscopic studies of field RHB chemical compositions were conducted by Tautvaišienė (1996, 1997) and Tautvaišienė et al. (2001). Those studies concentrated on thick disk and halo stars. Afşar et al. (2012) (hereafter ASF12) conducted a small-sample (76 star) survey of bright field stars with temperatures and luminosities consistent with RHB classification, identifying 18 probable true RHB stars, 13 of which appeared to be thin-disk solar metallicity (thus relatively young) objects.

Expanding on this unexpected result, we have recently reported an optical high-resolution spectroscopic survey of 340 field RHB candidates Afşar18a. This study used equivalent width (EW) measurements to derive model atmosphere parameters, metallicities, and some α -group and Fe-group abundance ratios. In Afşar18a, kinematics were computed for almost the entire sample from data in the Hipparcos and Gaia DR1 (Gaia Collaboration et al. 2016) catalogs. Based only on these data, we estimate that about 150 of the Afşar18a sample are true RHB stars, and that there is an admixture of thin and thick-disk members in the sample. In Afşar et al. (2018b) we will present abundances of elements requiring synthetic spectrum computations: odd-Z, Fe-group, neutron capture (n -capture) elements, and the light LiCNO group. We will also be able to refine the stellar evolutionary and Galactic population breakdown of this sample.

Optical high-resolution spectra are useful for stellar metallicities and relative abundance ratios of many elements, but they have limitations particularly among the lighter elements. Such deficiencies can be overcome by obtaining data in the infrared (IR) spectral domain, $\lambda > 1 \mu\text{m}$. To this end we have initiated a program to observe a large subset of the Afşar18a sample in the photometric H and K bands with the Immersion Grating Infrared Spectrometer (IGRINS). With these spectra we will be able to study light elements either not available or poorly studied in the optical spectral range (P, S, and K), greatly refine the abundances of those with some transitions in both the optical and IR regions (α elements Mg, Si, and Ca; odd-Z elements Na and Al; n -capture elements Ce, Nd, Yb), and most importantly improve the abundances of CNO and the carbon isotopic ratios derived from our optical data.

In this paper, we present IGRINS observations of three RHB stars from Afşar18a (also previously investigated in ASF12): HIP 54048, HIP 57748 and HIP 114809. We discuss atomic line identifications in the IGRINS data and the transition parameters of the chosen lines. A detailed comparison is made between the resulting abundances and those derived from the optical spectra. A future paper will contain the results from the full IGRINS survey, about 70 stars. In §2 the IGRINS observations and their reductions are described. In §3 we present the model atmosphere parameters and abundances of elements derived from the optical spectral region. Abundance determinations from the IGRINS H and K band spectra are described in §4 along with the atomic and molecular data used in abundance determinations. In §5 we investigate the infrared Fe I lines as temperature indicators. Finally, we discuss and summarize our results in §6.

2. OBSERVATIONS AND DATA REDUCTION

High-resolution, high signal-to-noise ($S/N > 200$ per resolution element) spectra of HIP 54048, HIP 57748 and HIP 114809 were obtained with IGRINS on the 2.7m Harlan J. Smith Telescope (HJS) at McDonald Observatory. The data were gathered in 2014 during an instrument commissioning run on May 24 and 27, and then on a separate run on October 19. We summarize the basic parameters and observation log in Table 1.

An important capability of IGRINS is that it obtains the complete coverage of H and K bands at high resolving power ($R \equiv \lambda/\Delta\lambda \simeq 45,000$) simultaneously without any adjustments to the instrument components. In a single exposure, the data cover a wavelength range between 14,800–24,800 Å, with a small gap of about 100 Å between bands. More detailed and extended descriptions of IGRINS are given in Yuk et al. (2010) and Park et al. (2014). A discussion of our observational techniques and reduction processes is given in Afşar et al. (2016) (hereafter Afşar16). Figure 1 and Figure 2 shows the ready-for-analysis spectra of three RHB stars: wavelength-calibrated, continuum-normalized, telluric-line-removed, and merged into a single continuous spectrum. We have restricted the figures in both H and K band wavelengths so that the heavily sky-contaminated band edges that were not used in the analysis are not shown. We also present a detailed spectral atlas for our stars taking HIP 54048 as the benchmark of RHB stars. A portion of the atlas is illustrated in Figure 3 (the complete figure is available online).

The optical spectra of HIP 54048, HIP 57748 and HIP 114809 were obtained during observing runs in 2009 and 2010, and their analyses were first presented in ASF12 and refined in Afşar18a. The details of the optical observations

and data reduction are described in that paper.

3. MODEL ATMOSPHERIC PARAMETERS AND ABUNDANCES FROM OPTICAL-REGION SPECTRA

Stellar atmospheric parameters of our program stars have been recently revisited by Afşar18a. Highlights of the new analyses include: (a) revision of the model atmospheric parameters by including the neutral and ionized species of Ti lines in the calculations along with Fe I and Fe II lines, and (b) updates to the line oscillator strengths from recent laboratory work. Afşar18a derived T_{eff} , $\log g$, $[\text{Fe}/\text{H}]$, and ξ_t using a semi-automated iterative driver operating on the current version of the local thermodynamic equilibrium (LTE) line analysis and synthetic spectrum code MOOG (Snedden 1973)³. In this study we adopt these revised model atmospheric parameters; they are listed in Table 2.

Atomic and molecular lines that we used to derive both atmospheric parameters and individual element abundances from the optical spectra are as described in Böcek Topcu et al. (2015) and Böcek Topcu et al. (2016). The line list used in this study is given in Table 3 along with oscillator strength information and references.

In total, we derived the elemental abundances of 21 species of 18 elements in the optical region by using EW measurements and spectrum syntheses (SYN) for those lines with hyperfine (HFS) structures and/or blending features. The abundances of elements Si, Ca, Ti, Cr, and Ni that were determined from EWs are taken from Afşar18a; details about those calculations are given below in §3.1. To find the differential abundances relative to the Sun, we adopted solar abundances from Asplund et al. (2009). The individual abundances are given in Table 3, and average $[\text{X}/\text{Fe}]$ values along with standard deviations and numbers of lines for all species are summarized in Table 4, 5 and 6.

3.1. α and Odd-Z Light Elements

We determined the abundances of α elements Mg, Si, S and Ca from their neutral species transitions. Abundances of Si and Ca were derived from EW measurements, while SYN was applied to determine Mg and S abundances.

There are only a few useful Mg I lines in the optical spectral region. Mg abundances in our stars were determined from two strong Mg I lines at 5528.4 and 5711.1 Å. They are slightly overabundant in all three stars, with little star-to-star scatter: $\langle[\text{Mg}/\text{Fe}]\rangle = +0.16$. Considering the large strength of these transitions, their derived abundances are very dependent on microturbulent velocities and other outer-atmosphere line formation effects.

Si is significantly overabundant in all three RHB stars, $\langle[\text{Si}/\text{Fe}]\rangle = +0.24$. There are 13-14 Si I lines participating in the analysis of each star, so statistically the Si abundance should be well determined. However, in Afşar18a we cautioned that the derived Si abundances are nearly always high, even in solar-metallicity stars. Moreover, there is a relatively large star-to-star scatter, and a significant trend with T_{eff} ; see Afşar18a Figure 13. We recommend caution in interpreting these Si abundances.

Optical S lines are rarely studied. We derived the S abundances for our RHB stars using the triplet centered at 6757.0 Å. Takeda et al. (2016) investigated non-local thermodynamic equilibrium (nLTE) effects for this triplet in G-K giant stars, finding corrections to be mostly $\lesssim 0.1$ dex, in good agreement with earlier computations (Korotin 2009). Sulfur abundances in our stars are essentially solar, $\langle[\text{S}/\text{Fe}]\rangle = +0.09$. Other studies have mostly used the S I transitions at 8693–5 Å. We could not study these lines because they fall into an echelle order gap in our spectra.

There are many Ca I lines in the optical wavelength region, and Afşar18a uses 11 of them. The resulting abundance is slightly above solar, $\langle[\text{Ca}/\text{Fe}]\rangle = +0.12$. In total, Mg, Si, S, and Ca all indicate $[\alpha/\text{Fe}] \simeq +0.15$, consistent with overall $[\alpha/\text{Fe}]$ levels in these mildly metal-poor disk stars (see Figure 14 of Afşar18a).

We derived the abundances of three light odd-Z elements, Na, Al, and K using the SYN method. Na abundances were usually determined from four Na I lines located at 5682.6, 5688.2, 6154.2 and 6160.6 Å. As is known from several studies (e.g. Takeda et al. 2003; Lind et al. 2011), these lines are subject to nLTE effects. Takeda et al. (2003) suggest that the Na I lines at 6154.2 and 6160.8 Å are the least sensitive to the nLTE effects, and the corrections needed for stars like our RHB stars are less than -0.1 dex, while the lines at 5682.6 and 5688.2 Å need nLTE corrections up to about -0.15 dex. These results are also in good agreement with Lind et al. (2011), who studied the nLTE calculations for neutral Na lines in late-type stars. With these recommended nLTE corrections, all four Na I lines yielded internally consistent abundances for each of the program stars. However, there is large star-to-star scatter, with HIP 54048, HIP 57748, and HIP 114809 giving abundances $[\text{Na}/\text{Fe}] = +0.25, +0.03, \text{ and } +0.34$, respectively.

For Al abundances we used neutral species transitions at 6696.0, 6698.7, 7835.3 and 7836.1 Å. Recently Nordlander & Lind (2017) have investigated nLTE effects on several Al I lines, including the ones we report in this study. They conclude that the nLTE corrections needed for the Al I doublets at $\lambda\lambda 6696, 6698$ and $\lambda\lambda 7835, 7836$ are not more than -0.05 dex for cool giants with solar metallicities. As in the case of Na, the internal line-to-line scatter is small for the

³ Available at <http://www.as.utexas.edu/~chris/moog.html>

four Al I transitions but the star-to-star scatter is substantial: $[\text{Al}/\text{Fe}] = +0.05, -0.15, \text{ and } +0.10$ for the three stars listed as above. Thus it appears that HIP 57748 has 0.2-0.3 dex smaller Na and Al abundances than do the other two stars.

The only available optical K I lines are those of the resonance doublet at 7665 and 7699 Å. Usually the 7665 Å line is too blended with the telluric A band to be of any use in abundance analyses. These very strong lines are severely affected by uncertainties in microturbulent velocities, adopted damping constants, and large nLTE effects (Takeda et al. 2002). Investigation of the K I 7699 Å line in our stars yielded ~ 0.6 dex higher abundances in all RHB stars compared to that expected for disk stars ($-1.0 \lesssim [\text{Fe}/\text{H}] \lesssim 0.0$) (see Figure 4 in Takeda et al. 2002 and Figure 6 in Takeda et al. 2009). Those two papers report nLTE corrections (Δ_{nLTE}) up to -0.7 dex. In a more recent study, Mucciarelli et al. (2017) also suggest Δ_{nLTE} corrections up to ~ -0.6 dex. Applying these large nLTE corrections bring our derived K abundances into reasonable agreement with the solar values.

3.2. Fe-group and neutron-capture elements

The Fe-group elements investigated in this study are Sc, Ti⁴, Cr, Co, and Ni. Abundances from Ti I, Ti II, Cr I, Cr II, and Ni I transitions were determined in Afşar18a using EW matching. Ti abundances from both neutral and ionized species were also used to help derivations of model atmospheric parameters. Sc and Co abundances were not reported in Afşar18a because Sc II and Co I lines have significant HFS substructure, and abundance extractions from them need special treatment. For these elements here we have used MOOG’s *blends* option that produces EWs from complex spectral features. Recent lab data for Co I are taken from Lawler et al. (2015). For Sc II lines we adopted the lab $\log gf$ values from Lawler & Dakin (1989). Abundances of the Fe-group elements appear to be mostly solar in all RHB stars, with the exception of modest deficiencies observed in Ti and Sc in HIP 57748, and a slight Sc overabundance in HIP 114809.

In this study, we have only investigated the neutron-capture (*n*-capture) elements Ce and Nd. Some other *n*-capture elements present in the optical spectra of these stars will be reported in the next survey paper Afşar et al. (2018b). Ce and Nd are two *n*-capture elements whose solar system abundances are due mostly to relatively slow *n*-capture events (the *s*-process). We determined the optical Ce abundances from four Ce II lines. The lab $\log gf$ data are taken from Lawler et al. (2009). Nd abundances were measured from two Nd II lines at 5255.5 and 5319.8 Å. Their lab data were gathered from Den Hartog et al. (2003). The abundances determined from the SYN method of both $[\text{Ce}/\text{Fe}]$ and $[\text{Nd}/\text{Fe}]$ vary from star to star in our small sample: slightly overabundant in HIP 54048, around solar in HIP 114809, and more than -0.2 dex deficient in HIP 57748.

3.3. The CNO Group

We determined CNO abundances by application of the SYN method to complex atomic and molecular features. To derive C abundances we analyzed CH G-band Q-branch band head lines in the 4300–4330 Å region and lines of the C₂ Swan band heads near 5160 and 5631 Å.

C abundances can be also derived from C I high excitation potential ($\chi \gtrsim 7.7$ eV) lines, and ASF12 attempted to apply *EW* analyses of them for their initial sample of RHB stars. The drawbacks of these lines include rapid decrease in strength with decreasing T_{eff} and probable nLTE effects. Here we determined C abundances from SYN analyses of three high-excitation C I lines that have been used in previous studies (e.g. Caffau et al. 2010) located at 5052.1, 5380.3 and 8335.1 Å. We list the individual line by line $\log \epsilon$ values in Table 7. The line-to-line scatter among the C I lines remains within ~ 0.1 dex.

For N abundances we analyzed the 7995–8040 Å region that contains ¹²CN and ¹³CN red system lines. The same region was also used to derive carbon isotopic ratios (¹²C/¹³C). O abundances were derived from two forbidden lines: [O I] 6300.3 Å and [O I] 6363.8 Å.

CNO abundances of our targets were previously investigated by ASF12. The results we report in this study are updated abundances (Table 4, 5 and 6) using the revised model atmosphere parameters from Afşar18a (Table 2) and different solar abundances from those of ASF12. Here we are using the Asplund et al. (2009) recommended CNO abundances $\log \epsilon(\text{C})_{\odot} = 8.43$, $\log \epsilon(\text{N})_{\odot} = 7.83$, and $\log \epsilon(\text{O})_{\odot} = 8.69$, instead of the ASF12 values of 8.38, 8.2, and 8.64, respectively. Comparison of these two solar CNO abundance sets is difficult because Asplund et al. used several abundance indicators for each element and a variety of analytical approaches, while ASF12 concentrated on CH, CN, and [O I] using SYN as in the present work. A closer comparison would be the lab/solar/stellar study of Sneden et al. (2014), who derived $\log \epsilon(\text{C})_{\odot} = 8.48$, $\log \epsilon(\text{N})_{\odot} = 8.05$, and $\log \epsilon(\text{O})_{\odot} = 8.69$, which essentially agrees with Asplund

⁴ Ti is often classified as an α element. The major naturally-occurring isotopes of true α elements Mg, Si, S, and Ca are composed of multiples of ⁴He nuclei. However, the Ti abundance is dominated by ⁴⁸Ti (73% in the solar system), and the α isotope ⁴⁴Ti is unstable with a short half-life. Ti is better classified as a Fe-peak element.

et al. for C and O, but has a 0.2 dex larger N abundance. The difference in adopted solar N abundance is larger between ASF12 and Asplund et al.: $\Delta \log \epsilon(\text{N}) = \log \epsilon(\text{N}_{\odot})_{\text{ASF12}} - \log \epsilon(\text{N}_{\odot})_{\text{Asplund}} \simeq 0.4$ dex, which leads naturally in a large difference in our [N/Fe] values compared to those of ASF12. Lower metallicity values (-0.13 dex on average) in the Afşar18a revised model atmospheres of all RHB stars also contribute to [X/Fe] offsets for the CNO group. The reader should keep these differences in mind in interpretations of these elemental abundances.

Scale differences between the present work and that of ASF12 do not change the general conclusions about the CNO group. Their abundances follow the general trends of evolved disk giants: C abundances decrease, while N abundances increase due to convection movement of the CN-processed material from inside out to the stellar surface, and O holds its own essentially solar value.

We also determined carbon isotopic ratios from the primary $^{12}\text{C}/^{13}\text{C}$ indicator near 8004.7 \AA , which is a triplet of ^{13}CN lines. In the left panels of Figure 4 we illustrate the weakness of ^{13}CN absorption in our relatively warm RHB stars. As previously reported in ASF12, a meaningful value of $^{12}\text{C}/^{13}\text{C}$ of HIP 114809 in the optical region could not be derived. We list the derived ratios in Table 10; these will be discussed further in §4.4.

4. ABUNDANCES FROM IGRINS NEAR-INFRARED SPECTRA

High-resolution, high signal-to-noise *H* and *K* band spectra of RHB stars reveal a rich assortment of atomic and molecular features (Figure 3).

Having this opportunity, we were able to compute the abundances of 21 species of 20 elements along with $^{12}\text{C}/^{13}\text{C}$ ratios. For our three RHB stars, abundances of P, S, and K were obtained for the first time. All abundances and $^{12}\text{C}/^{13}\text{C}$ ratios were derived by applying SYN method to the observed spectra. The atomic and molecular data used for abundance calculations and the abundance analysis of all species are discussed in the following subsections. In all cases the individual line abundances are given in Table 3 and the abundance summaries for the stars are given in Tables 4, 5, and 6.

4.1. Atomic and molecular data

We adopted the molecular data described in Afşar16 (and references therein) for CN, CO, and OH features, and generated the atomic line list (Table 3) following a similar procedure to that of Afşar16. We used the Arcturus infrared atlas (Hinkle et al. 1995)⁵ along with atomic line lists from the National Institute of Standards and Technology (NIST) Atomic Spectra Database⁶ and from the Kurucz (2011) database⁷ to identify promising atomic lines in our RHB stars. Accurate transition probability information for the atomic and molecular data is essential for a robust abundance analysis. For lines that have NIST transition probabilities rated A and B accuracy (uncertainty $\leq 10\%$), we adopted the NIST $\log gf$ values. However, laboratory transition probabilities for most of the species transitions in the *IR* are lacking. Therefore, we had to apply reverse solar analyses to determine the “astrophysical” $\log gf$ values of mostly neutral-species of elements listed in Table 3. Only a few ionized-species could be identified (see §3.2), and among them we only applied reverse solar analysis to Yb II. The transition probabilities ranked as C (accuracies $< 20\%$) in the NIST database were needed to be justified in most of the cases with their own reverse solar analyses. The sources of all transition probabilities are provided in Table 3.

For the reverse solar analyses we used the high-resolution infrared solar flux spectrum of Wallace & Livingston (2003), and adopted the solar model atmosphere of ASF12. The derived transition probabilities then were tested on the Arcturus atlas spectra (Hinkle et al. 1995), adopting the Arcturus abundances and model atmospheric parameters from Ramírez & Allende Prieto (2011). Satisfactory agreement with the abundances derived by Ramírez & Allende Prieto was achieved for all the elements investigated in this manner.

Applying reverse solar analysis to obtain astrophysical oscillator strengths comes with its own handicaps. Barklem et al. (2000) computed collisional broadening cross-sections for many neutral species transitions in *UV* and optical spectral regions, but their work stops short of the *H* and *K* band regions. Broadening cross-sections of Fe II lines in the *H* and *K* bands have been provided by Barklem & Aspelund-Johansson (2005), but these transitions are too weak to be detected for our RHB IGRINS data. Therefore, we had to resort initially to the classical Unsöld (1955) approximation, which is known to underestimate the observed line broadening due to van der Waals interactions (e.g. Chen et al. 2000). This approximation especially has difficulties in transitions that occur at higher-excitation potentials ($\chi_{\text{low}} > 3.0$ eV, Chen et al. 2000, and references therein), which is mostly the case in our lines. Thus, we applied a damping enhancement factor of about 3.2 on average to the van der Waals damping computed according to the Unsöld approximation in order to better estimate the collisional broadening effect on absorption lines. Although

⁵ Available at <ftp://ftp.noao.edu/catalogs/arcturusatlas/>

⁶ https://physics.nist.gov/PhysRefData/ASD/lines_form.html

⁷ <http://kurucz.harvard.edu/linelists.html>.

applying enhancement factors temporarily cure the problem in an empirical way, the underlying physics of the strong broadening we observe in the lines of the infrared solar spectrum should be investigated in the future.

We compare our astrophysical oscillator strengths with the ones reported by [Shetrone et al. \(2015\)](#) for the APOGEE high resolution H -band spectroscopic survey ([Majewski et al. 2016, 2017⁸](#)) for the 40 lines in common in both studies in Figure 5: 13 Fe, two Ti, seven Si, two P, three S, two K, four Ca, two Cr and five Ni (all neutral species transitions). As seen in the figure, the astrophysical oscillator strengths from both studies are mostly in good agreement within $\sigma = 0.12$ dex. We also compared our damping parameters with the ones reported by [Shetrone et al. \(2015\)](#), in which they also predict enhanced damping for most of the IR lines in common. They define the damping parameter as: $\text{vdW} = \log(\Gamma_6/N_H)$; Γ_6 is the van der Waals collisional damping and N_H is the number density of hydrogen. Comparison of our vdW values with [Shetrone et al.](#) resulted in reasonable agreement, $\langle \text{vdW} \rangle = -0.02$ ($\sigma = 0.25$).

4.1.1. Isotope Shift in Ti I

To the best of our knowledge, Ti I lines are the only ones whose IR profiles have been investigated in detail. [Blackwell-Whitehead et al. \(2006\)](#) called attention not to damping effects, but to isotopic wavelength splits. They found that Ti I IR lines have significant isotopic broadening. Although most of Ti is in the form of ^{48}Ti , it has five naturally-occurring isotopes: ^{46}Ti , 8.25%; ^{47}Ti , 7.44%; ^{48}Ti , 73.72%; ^{49}Ti , 5.41%; and ^{50}Ti , 5.18%.⁹

Isotope shifts (ISs) in Ti I, like other spectra, are due to a combination of Normal Mass Shift (NMS), Specific Mass Shift (SMS), and Field Shift (FS). The NMS is the elementary reduced mass shift of classical or quantum mechanical two body systems. Elements near the top of the periodic table have dominant NMSs starting with H I vs D I ISs. The SMS arises from terms in the Hamiltonian involving the momentum of one electron dotted with the momentum of another electron. Multi-electron atoms, including Ti, can have significant SMSs. Lastly the FS appears from changes in the mean squared charge radius of the nucleus as neutrons are added. In general one finds large ISs near the top of the periodic table dominated by mass shifts, and large ISs near the bottom of the periodic table dominated by FSs especially when there is an s-electron participating in the atomic transition.

The important Fe-group spectra tend to have small ISs that are difficult to detect in stellar spectra. However, this situation may change due to the development of HgCdTe detector arrays and the increase in high spectral resolution, high S/N stellar data. The study of atomic transitions at lower frequencies, e.g. in the IR, will generally yield larger fractional ISs. Data in this work on the IR lines of Ti I clearly reveal ISs. Studies of pre-solar grains in chondrites have revealed many variations in isotopic abundance patterns (e.g. [Lodders & Amari 2005](#)) that result from different nucleo-synthetic histories of grain material. The possibility that the IR may enable more detailed studies of isotopic abundance patterns using stellar spectra is appealing.

We recorded the Ti I ISs in the laboratory using the NIST 2-m Fourier Transform Spectrometer (FTS) and a high-current hollow cathode lamp. Although our laboratory studies are limited to data from FTS, there have been laboratory studies of ISs in Ti I employing narrow band lasers ([Azaroual et al. 1992, Anastassov et al. 1994, Luc et al. 1994, Gangrsky et al. 1995, Luc & Vetter 1996, Furmann et al. 1996, Jin et al. 2009](#)). Single frequency laser experiments can fully resolve HFS structure of the odd isotopes ^{47}Ti and ^{49}Ti . Small FSs in Ti I have been studied ([Azaroual et al. 1992, Anastassov et al. 1994, Luc et al. 1994](#)). A J-dependence of ISs for lines in a single multiplet have been detected and studied ([Gangrsky et al. 1995](#)). Such J-dependences are typically quite small changes in ISs that are already small, but do occur due to mixing of levels. Negative ISs, in which the heavier isotopes are the red of the lighter isotopes, were clearly observed and explained by [Luc & Vetter \(1996\)](#). The dominance of the SMSs in the ISs of $3d^3 4s a^5F - 3d^2 4s4p y^3F$ is responsible for negative ISs as demonstrated using Hartree-Fock calculations by [Luc & Vetter](#). Of our 10 Ti I IGRINS lines, the six longest wavelength transitions belong to the $3d^3 4s a^5P - 3d^2 4s4p z^5D$ multiplet and exhibit the negative ISs explained by [Luc & Vetter](#) in terms of the SMSs of $3d - 4p$ transition. In our FTS data we find the $^{49,50}\text{Ti}$ isotopes of these lines at $-0.0430 \pm 0.0108 \text{ cm}^{-1}$ with respect to the dominant ^{48}Ti isotope and the $^{46,47}\text{Ti}$ isotopes at $+0.0430 \pm 0.0132 \text{ cm}^{-1}$ with respect to the dominant ^{48}Ti isotope. We are not able to detect any J-dependence in our FTS data on this IR multiplet. For all of its transitions, in our laboratory spectra we are unable to resolve the minor odd isotopes ^{47}Ti and ^{49}Ti from their even isotope companions ^{46}Ti and ^{50}Ti , respectively. Since we could not definitively separate the contributions to the shifts from the even isotopes, we quote the combined shift due to both isotopes. An example laboratory spectrum for one of the Ti I IR lines is presented in Figure 6. In solar-system material the four minor isotopes are about equal abundance, and are displaced nearly symmetrically to the blue and red of ^{48}Ti as seen in this figure, and the wavelength shifts are fractions of the total line widths in stellar spectra. Therefore an isotopic mix very different from the solar system would be needed in another

⁸ <http://www.sdss.org/dr14/irspec/#APOGEEsurveyandInstrumentsOverview>

⁹ Chang, J.: Table of Nuclides, KAERI(Korea Atomic Energy Research Institute). Available at: <http://atom.kaeri.re.kr/ton/>. Retrieved June 11, 2018

star to detect noticeable line asymmetries.

The next two shorter wavelength transitions in our IGRINS data, at 17376 Å and 17383 Å, connect rather high lying levels of neutral Ti and do not have sufficient S/N in our FTS data for extracting ISs.

The two shortest wavelength Ti I transitions in our IGRINS data, at 15543 Å and 15602 Å, are the $3d^3 4s a^3G_4 - 3d^2 4s4p z^3G_4$ and $3d^3 4s b^1G_4 - 3d^2 4s4p z^1G_4$ lines. These lines also have negative ISs but they are not as well resolved in our FTS data. This illustrates the smaller fractional ISs as the optical wavelength region is approached. We find the $^{49,50}\text{Ti}$ isotope shift for the 15543 Å line to be $-0.0396 \pm 0.0050 \text{ cm}^{-1}$ with respect to the dominant ^{48}Ti isotope and the $^{46,47}\text{Ti}$ isotope shift to be $+0.0408 \pm 0.0050 \text{ cm}^{-1}$ with respect to the dominant ^{48}Ti isotope. For the 15602 Å line, the $^{49,50}\text{Ti}$ shift with respect to ^{48}Ti is $-0.0356 \pm 0.0056 \text{ cm}^{-1}$, and the $^{46,47}\text{Ti}$ shift with respect to ^{48}Ti is $+0.0361 \pm 0.0092 \text{ cm}^{-1}$.

Embedding this Ti I isotopic structure into the atomic line list cures the broadening observed at the wings of these weak lines in the solar spectrum, providing a more robust test bed for the oscillator strengths reported by Blackwell-Whitehead et al. (2006). We applied the log *gf* values of Blackwell-Whitehead et al. to the solar spectrum for the seven lines in common (except for the Ti I line at 15602.84 Å) and remeasured the solar Ti abundance. These computations indicated that the abundances from two of the lines at 15543.76 and 21782.94 Å result in a considerable amount of offset from the Ti abundance reported by Asplund et al. (2009) ($\log \epsilon(\text{Ti})_{\odot} = 4.95$), with the latter suggesting about 0.25 dex lower Ti abundance in the Sun. Therefore, to achieve internally consistent Ti abundances in the Sun, Arcturus and our stars we opted to apply reverse solar analysis to all Ti I lines we list in Table 3. Our astrophysical log *gf* values stay nearly within the log *gf* uncertainties given by Blackwell-Whitehead et al., except for the two lines mentioned here.

4.2. α and Odd-Z elements

Molecular lines become major contributors in the spectrum of cool stars towards longer wavelengths. As a result, the near-*IR* spectra contains many molecular lines, mainly CN, OH and CO. Therefore, applying the SYN technique is advisable for all *IR* features of this study.

We derived the abundances of α elements Mg, Si, Ca and S from their neutral species transitions. We plot example Mg, Ca and S lines in HIP 54048 in Figure 7. The line-by-line α abundances for HIP 54048 are displayed in Figure 8. We also include in this figure α -like Ti, for which we have both neutral and ionized species transitions. By inspection it is clear that the abundances from lines in the *H* and *K* bands are in accord with their optical counterparts. This conclusion is confirmed by the abundance statistics of Tables 4–6. The *IR* abundances often have better internal self-consistency compared to optical ones. Additionally, for some elements the *IR* abundances may be preferable to the optical ones. For example, we were able to use 11 Mg I lines in the infrared but only two could be used in the optical. The 5528 and 5711 Å lines are both very strong in our RHB stars. For HIP 54048, their reduced equivalent width RW ($\equiv \log(\text{EW}/\lambda)$) values are -4.4 and -4.7 , respectively. This means that both are well up on the flat part of the curve-of-growth, relatively insensitive to Mg abundances. However, the *IR* Mg I lines include several on the linear part of the curve-of-growth; we trust the *IR* Mg results.

We report S abundances for our program stars for the first time. Considering the importance of this element for the cosmochemical evolution of the Galaxy, it is important to compare the abundances derived from S I lines in the *IR* to their very few optical counterparts. There are 10 useful S I lines available in *H* and *K* bands for our RHB stars (Table 3).

The four true α elements have virtually the same abundance levels. Defining $\langle[\alpha/\text{Fe}] \equiv [\text{Mg}, \text{Si}, \text{S}, \text{Ca}/\text{Fe}] \rangle$, we find that $\langle[\alpha/\text{Fe}] \simeq 0.15$ with $\sigma \simeq 0.08$ in all three RHB stars in both optical and *IR* spectral regions.

The abundances of odd-Z elements Na and Al were also obtained from the near-*IR* lines (Figure 10). Additionally, we were able to measure the abundances of another two odd-Z elements, P and K, for the first time for our targets.

Na abundances were determined from Na I lines at 22056.4, 22083.7, 23348.4 and 23379.1 Å. The log *gf* values of Na lines are quite well determined as listed in the NIST database (ranked A+). The transitions at 23348.4 and 23379.1 Å on average, give about 0.1 dex higher abundances in all RHB stars (Table 3, Figure 10) than do other Na I lines. The 23348.4 Å line is also partly blended with a CO line. Additionally, the effects of nLTE on these lines are yet to be investigated. The Na abundances obtained from the *IR* are in agreement with the optical Na abundances and show the same trend in all RHB stars. Na abundances are well enhanced in HIP 54048 and HIP 114809 by $[\text{Na}/\text{Fe}] > 0.25$ dex. HIP 57748, on the other hand, has solar Na abundance.

Al abundances were measured from six Al I lines; two in the *H*, and four in the *K* band. When compared to other elements investigated in this section, the Al abundances indicate a higher line-to-line scatter ($\sigma \simeq 0.1$ dex), and the *K* band Al lines are the main contributors to this scatter. *H* band Al abundances from 16763.4 and 17699.0 Å

lines are usually in agreement with the optical results. The average infrared Al abundance is always ~ 0.1 dex higher compared to the average optical Al abundance in case of all RHB stars, with slight overabundances in HIP 54048 and HIP 114809.

The most commonly used P lines for abundance calculations are the P I *UV* doublet, 2135/2136 Å (e.g. Jacobson et al. 2014; Roederer et al. 2014) and two near *IR* P I lines at 1050–1082 nm (e.g. Caffau et al. 2011; Maas et al. 2017). In this study, we report the abundances from two different near-*IR* lines located in the *H* band: 15711.5 and 16482.9 Å (Figure 9). We could not derive an abundance from the 16482.9 Å line for HIP 114809. It is too weak in our IGRINS spectrum, and only an upper limit could be derived from the P I line at 15711.5 Å. P abundances are estimated to be at solar values in all RHB stars.

H band data provide two K I lines at 15163.1 and 15168.4 Å (Figure 9). This region, however, is fairly contaminated by the CN molecular lines that can be seen in the figure. Nevertheless, they provide K abundances around solar as expected from mildly metal-poor and solar metallicity stars (e.g. Takeda et al. 2002, 2009). As discussed in §3.1, nLTE effects on the optical lines are severe and the K abundances obtained from those lines are about 0.6 dex higher than the solar value. Considering the K abundances we determined from the *H* band lines, we suggest that 15163.1 and 15168.4 Å K I lines may provide less nLTE-affected abundances.

4.3. Fe-group and neutron-capture elements

Abundances of the same Fe-group elements discussed in §3.2 were also determined from the *IR* lines of Sc, Ti, Cr, Co and Ni (Figure 10). Here we also give the Fe abundances from the Fe I lines identified in the *H* and *K* bands.

We could identify only two Sc I lines in the *K* band: 22065.2 and 22266.7 Å. Recently, Pehlivan et al. (2015) measured the oscillator strengths for single atomic level transitions of Sc I lines and van Deelen (2017) studied the HFS structure of these lines in the near-*IR*. We adopted the oscillator strengths and HFS splittings from these studies and applied SYN analysis to our Sc lines. These lines are weak in our stars and we could only detect them in HIP 54048. Optical abundances were determined from Sc II lines. The results for HIP 54048 from both infrared and optical species have a small offset: $[\text{Sc II}/\text{Fe}]_{\text{opt}} - [\text{Sc I}/\text{Fe}]_{\text{ir}} = 0.15$. This discrepancy somewhat resembles the difference observed between the neutral and ionized species of Cr in the optical.

We identified 10 useful Ti I lines and one Ti II line at 15783 Å (Wood et al. 2014) in our IGRINS data. The abundances we obtained from the infrared are in accord with the ones obtained from the optical. Both the optical and *IR* Ti lines in HIP 57748 support a modest abundance deficiency: $[\text{Ti}/\text{Fe}] \simeq -0.15$. HIP 54048 and HIP 114809 have about solar Ti abundances. Although the general $[\text{Ti II}/\text{Fe}]$ abundance trend is the same both in the infrared and optical, there is a mean offset of about +0.16 dex between the abundances $[\text{Ti II}/\text{Fe}]_{\text{ir}}$ and $\langle [\text{Ti II}/\text{Fe}] \rangle_{\text{opt}}$ in all RHB stars.

The other Fe-group elements have general agreement between optical and *IR* transitions. Cr I lines and the abundances are about solar in all RHB stars. Note that there is just one Co I line identified at 16757.6 Å. Six Ni I lines were identified in the *H* band. The Ni abundances for all RHB stars are in good accord with the optical ones.

There are many Fe I lines in the both *H* and *K* bands (Figure 3). Here we only discuss the ones that are not heavily blended with other atomic and molecular features. In total, we were able to identify 27 Fe I lines in both bands. We applied both EW and SYN methods to measure the Fe abundances in our stars (please see §5 for further discussion on the EW method). In Tables 3–6 we only list the abundances obtained from the SYN method. In Table 9 we compare the Fe abundances derived from the same Fe I lines applying both methods. The agreement between the results from two methods is well within the uncertainty of 0.05 dex. Comparison of both optical: $\log \epsilon(\text{Fe I})_{\text{opt}} = 7.17$ (Afşar18a) and infrared: $\log \epsilon(\text{Fe I})_{\text{ir(SYN)}} = 7.18$ abundances results in a very good agreement. In §5 we discuss other aspects of the *IR* Fe I lines.

We derived the abundances of *n*-capture elements Ce, Nd and Yb from their ionized species transitions. We adopted the $\log gf$ values of Ce II from Cunha et al. (2017) and the $\log gf$ value for Nd II was taken from Hasselquist et al. (2016). Ce and Nd have been already discussed in §3.2, but Yb was detected only in the *H* band at 16498.4 Å. The commonly used near-*UV* Yb II resonance line at 3694 Å was unavailable for our RHB stars because it is too strong and lies in a very crowded, low-flux spectral region. In Figure 11, we display one Ce II line and the Yb II line in our stars. Yb is a *n*-capture element whose solar system abundance mainly comes from rapid *n*-capture (*r*-process) nucleosynthesis. Hawkins et al. (2016) detected the Yb II line in the Arcturus spectrum. As is seen in their Figure 13, the Yb line in Arcturus is considerably blended with a CO feature. However, this contamination is fairly weak in our stars due to their relatively high temperatures compared to Arcturus. Nonetheless, one needs to be aware of the potential CO contribution to the Yb line in cooler stars. Yb is essentially solar in all of our RHB stars, $\langle [\text{Yb}/\text{Fe}] \rangle \simeq +0.06$, while the *s*-process elements Ce and Nd exhibit large star-to-star scatter. This issue will be investigated further in a future

paper with a larger RHB sample.

4.4. The CNO Group

The *H* and *K* bands contain molecular bands of OH, CN and CO, which we used to determine the abundances of C, N and O. Since the CNO elements are tied together through molecular equilibrium, we applied an iterative SYN analysis for the CNO abundances as described in Afşar16. Since O is expected to be more abundant than C it should be less affected by CO formation, so we started with OH analyses to determine the O abundances. However, OH lines are very weak in these warm RHB stars. We were able to detect up to five useful OH transitions in our spectra. The OH region at ~ 16872 Å is given in Figure 12 for all RHB stars and Arcturus. The high-resolution Arcturus atlas (Hinkle et al. 1995) shows that there are in fact two distinct molecular OH features centered at ~ 16872 Å. The same features appear as blends in our stars. HIP 54048 has the lowest temperature ($T_{\text{eff}} = 5099$ K) of our stars and the OH feature at 16872 Å is better resolved compared to the one in HIP 57748 ($T_{\text{eff}} = 5307$ K) at the same metallicity. Although HIP 114809 spectrum has lower *S/N* and the lowest metallicity ($[M/H] = -0.38$) in our sample, its OH feature still is present. Abundances of O derived from the OH features in all three stars agree well with those obtained from the [O I] lines in the optical: $\langle [O/Fe]_{\text{opt}} - [O/Fe]_{\text{ir}} \rangle = 0.04$ dex (Table 4–6).

C abundances were determined from the numerous CO molecular lines in the *K* band (Figure 2). We started the abundance analysis by adopting the O abundance derived from OH lines. The C abundances obtained from the CO lines came out to be about 0.1 dex higher than the C abundances estimated from the CH lines and lines of the C₂ Swan band heads discussed in §3.3. This very small difference may be attributed to the larger temperature sensitivity of CO molecular line strengths (see Afşar16 for a detailed discussion). On the other hand, CH and C₂ molecular lines come with their own problems. They are very small constituents in the overall C molecular equilibrium, and they are known to be severely blended with atomic absorption features; all these factors bring difficulties in determination of C abundances. Considering that we can only work with the molecular features to determine C abundances in both optical and *IR* regions, the agreement in abundances obtained from both regions is reasonable.

In addition to the high-excitation potential C I lines investigated in §3.3, we located four useful C I lines at 16021.7, 16890.4, 17456.0, and 21023.2 Å in the near-*IR*. These lines are the ones least blended with surrounding features. First we collected the log *gf* values from the NIST database and applied them to the solar spectrum using the SYN method. Except for the C I line at 21023.2 Å, other log *gf* values provided solar C abundances about -0.11 dex lower than the abundance reported by Asplund et al. (2009). Applying NIST log *gf* values to our RHB stars and Arcturus, however, resulted in very good agreement with the C abundances obtained from CO features. The average C abundances from C I lines are, $\langle \log \epsilon(C) \rangle_{\text{NIST}} = 7.72, 8.16,$ and 7.84 for HIP 54048, HIP 57748, and HIP 114809, respectively. To ensure the internal consistency of this study, we decided to apply reverse solar analysis to the C I lines and obtained astrophysical log *gf* values for the lines at 16021.7, 16890.4, and 17456.0 Å. Applying astrophysical log *gf* values to our stars and Arcturus yielded C abundances, surprisingly, still in good agreement with the ones obtained from CO features. The average C abundances determined using astrophysical log *gf* values for our stars are $\langle \log \epsilon(C) \rangle_{\text{astro}} = 7.78, 8.21,$ and 7.90 for HIP 54048, HIP 57748, and HIP 114809, respectively. The C I line at 8335.1 Å in the optical and the *IR* lines at 16890.4 and 17455.9 Å increase the abundance scatter obtained from C I lines. Resolution of this issue is beyond the scope of our study. In a followup study we will perform a detailed investigation with a larger sample for better clarifying the behavior of the *IR* C I lines. Overall results for the C abundances from all individual species and the average values from the five species abundance indicators for the stars are listed in Tables 7 and 8.

We derived the N abundances from the CN molecular transitions in the *H* band. The C and O abundances derived from CO and OH lines were taken from the analyses described above. *H* band CN features provide relatively consistent N abundances with the ones obtained from the optical CN features.

Prominent features including band heads of the ground electronic state first overtone (2–0) and (3–1) R-branch vibration-rotation bands of ¹²CO (2–0) are accompanied by ¹³CO (2–0) features near 23440 Å and those of ¹³CO (3–1) at about 23730 Å. These CO bands offer the opportunity to derive more accurate ¹²C/¹³C ratios than possible with the weak ¹³CN bands in the optical region, as discussed in §3.3. This is illustrated in Figure 4 with side-by-side comparisons of CN (left panel) and CO (right panel) features. In Table 10 we list the derived ¹²C/¹³C values for the three RHB stars. Happily, the ratios derived from both molecules in fairly good agreement. Most importantly, the ¹³CO band head features let us prove that the HIP 114809 surface has been enriched with CN-cycle products ($\langle ^{12}\text{C}/^{13}\text{C} \rangle = 15$) which was not possible in ASF12. This improvement will allow one to redefine and constrain the ¹²C/¹³C ratios in a larger number of evolved stars, which in turn will bring more constraints on stellar evolution models.

5. FE I LINES IN THE INFRARED AS TEMPERATURE INDICATORS

To derive the model atmospheric parameters without having any information from the optical region is a difficult task. The most important starting point is to have an accurate value of effective temperature. Here, using our limited sample, we describe a couple of methods to estimate effective temperatures of stars using only the *IR* spectral features. The second paper of this study will also explore the methods to derive model atmospheric parameters using only the spectral features in the *IR* with a larger sample.

As mentioned earlier, spectral regions redward of about 7000 Å have substantial molecular features in G-K giant stars; truly unblended atomic absorption lines become increasingly difficult to find as wavelength increases. Nonetheless we searched for as many clean Fe I lines as possible in our IGRINS spectra, using the atomic data sources cited above and the Arcturus line list of [Hinkle et al. \(1995\)](#). We were able to identify about 25 relatively unblended Fe I lines in total. We first measured the EW values of these lines in Arcturus and derived individual line abundances, again adopting the atmospheric parameters from [Ramírez & Allende Prieto \(2011\)](#). As seen in the left panel of Figure 13 the derived Fe abundances show no obvious trends with excitation potential χ and with RW. The average abundance obtained from the EW measurements of infrared Fe I lines are in accord with the Fe abundance reported by [Ramírez & Allende Prieto](#): $\log \epsilon(\text{Fe})_{\text{EW}} = 6.96$ ($\sigma = 0.02$), and $\log \epsilon(\text{Fe})_{\text{Ramirez}} = 6.98$. We then applied the same procedure to our program stars. As an example, Fe line abundances for HIP 114809 are shown in the right panel of Figure 13. No obvious trends with χ and RW are seen. The average $\log \epsilon(\text{Fe})_{\text{ir}}$ values for our RHB stars (Table 9) are in good agreement with the $\log \epsilon(\text{Fe})_{\text{opt}}$. These efforts suggest that the infrared Fe I lines can be used to determine reliable stellar effective temperatures in the cases of no available data from the optical region.

We also applied [Fukue et al.](#) LDR relations to our stars and obtained $T_{\text{eff(LDR)}}$ values from eight pairs of absorption lines. We excluded the K I(15163.09)/Fe I(15244.97) pair in all three cases because it always yielded about 400 K higher temperature values compared to other absorption line pairs. The $T_{\text{eff(LDR)}}$ values we obtained by applying [Fukue et al.](#) method for our stars: HIP 54048, $T_{\text{eff(LDR)}} = 5157$ K ($\sigma = 123$ K); HIP 57748, $T_{\text{eff(LDR)}} = 5312$ K ($\sigma = 215$ K); HIP 114809, $T_{\text{eff(LDR)}} = 5235$ K ($\sigma = 151$ K). These are in excellent agreement with our optical spectroscopic T_{eff} values, being on average only about 50 K higher, well within the mutual uncertainties of both sets of measurements.

6. SUMMARY AND DISCUSSION

This paper is the first one of a series of papers that explores stellar atomic and molecular features of Galactic field RHB and red giant stars observed in the near-*IR* region. IGRINS high-resolution, high S/N *H* and *K* band spectra bring valuable new information for this purpose. Several important light elements are poorly studied (e.g., S and K) or not available (e.g., P) in high-resolution optical spectra. IGRINS near-*IR* spectra provide more robust abundance analysis for many elements.

We have conducted, for the first time, the abundance analysis of three RHB stars; HIP 54048, HIP 57748 and HIP 114809, using high-resolution, high S/N near-*IR* IGRINS spectra. Detailed abundance analyses were carried out for 21 species of 20 elements including α (Mg, Si, S and Ca); odd-Z (Na, Al, P and K); Fe-group (Sc, Ti, Cr, Co, Fe, and Ni); *n*-capture elements (Ce, Nd, Yb); and CNO group elements. We also used the ground electronic state first overtone ($\Delta v = 2$) R-branch vibration-rotation bands of (2–0) and (3–1), which are the prominent features in K-band spectra, to determine $^{12}\text{C}/^{13}\text{C}$ ratios from ^{13}CO (2–0) features near 23440 Å and ^{13}CO (3–1) features at about 23730 Å.

To perform the abundance analysis in the *H* and *K* band spectra, we adopted the model atmosphere parameters from Afşar18a. Using the high-resolution optical spectra of our RHB stars (ASF12), we also determined the abundances of the same elements (except for P) in the optical region. This broad wavelength coverage allowed us too make more comprehensive analyses of our stars.

The abundances of α elements obtained from both wavelength regions are generally in good agreement and, on average, they indicate α enhancements of about $\langle [\alpha/\text{Fe}] \rangle \simeq 0.15$ dex. Our IGRINS spectra yield substantial numbers of Mg and S lines with internally self-consistent abundance results (Figure 8). We have identified 11 Mg I lines in contrast to two optical Mg I lines that come with analytical difficulties due to their large absorption strengths. The *IR* Mg I lines now give us more robust Mg abundances in these stars. Being located closer to the linear part of the curve-of-growth than the two optical lines, we trust the abundances of Mg obtained from the *IR* Mg I lines (Figure 7).

Sulfur is one of the fundamental building block elements of life in the universe along with C, H, N, O and P. Sulfur and sulfur-containing compounds are common constituents in Solar System material. High amounts of sulfur are produced in supernova nucleosynthesis during explosive oxygen burning ([Truran 1973](#)). Sulfur is volatile with its low condensation temperature; it can not be condensed into interstellar dust grains. Therefore, its depletion-free nature makes sulfur a valuable tracer of Galactic nucleosynthesis; understanding of its contribution to Galactic chemical evolution is important. There have been a number of studies that investigate the behavior of S in the Galaxy as one

of the α elements. Different investigations claim different results. Some suggest that S behaves like other α elements, showing a [S/Fe] *plateau* at certain metallicities, while others indicate that [S/Fe] has a linear increase with decreasing metallicities (e.g. Caffau et al. 2005, and references therein). There are few well-known S I lines in the optical and shorter wavelengths of near-*IR*: 6743–6757 Å optical multiplet, 8694–5 Å, 9212–9237 Å *IR* triplet, and 10455–9 Å *IR* triplet. Most of these lines were investigated by Korotin (2009) and Takeda et al. (2016) for their being subjected to nLTE effects. All these S lines appear to need nLTE corrections in different amounts, 6743–6757 Å optical multiplet having the smallest (to -0.10 dex) nLTE correction among others.

IGRINS provides more S I lines beyond those of the optical and very near-*IR*. We were able to identify 10 useful *H* and *K* band S I lines. We also measured the S abundance using the optical triplet centered at 6757.0 Å. The internal abundance self-consistency of all S I lines is encouraging. The *IR* S lines are mostly weak and likely to be less affected by nLTE conditions. These lines, studied here for the first time in these stars, promise to provide more robust investigation at a range of metallicities. In the forthcoming paper of this series, we will investigate S in more detail with a larger sample.

The abundances of odd-*Z* elements Na, Al, P and K were computed from both optical (when available) and infrared regions. Optical transitions of these elements are subject to substantial nLTE corrections (e.g. Takeda et al. 2002, 2003; Lind et al. 2011; Nordlander & Lind 2017; Mucciarelli et al. 2017). Among these, optical Al I lines used in this study are the least affected ones by nLTE, while K I at 7699 Å is the most affected, by up to -0.7 dex (Takeda et al. 2002, 2009). This is also found in our stars (Tables 4–6).

The Na abundances obtained in both wavelength regions are in good agreement in all three RHB stars but the star-to-star scatter is substantial. Even with nLTE corrections to the optical Na I lines, overabundances observed in both HIP 54048 and HIP 114809 remain. The good agreement between the optical and *IR* Na abundances suggests that all of these lines might be affected by nLTE conditions about the same amount. A similar situation is also observed in Al abundances from both regions. HIP 54048 and HIP 114809 also show slight Al overabundances, reminiscent of the well known [Na/Fe]-[Al/Fe] correlation observed in globular clusters (e.g. Kraft 1994 and references therein).

Phosphorus is one of the fundamental building blocks of life but its nucleosynthetic origin is still under discussion. Recent studies point to massive star explosions (hypernova, e.g., Kobayashi et al. 2006; Cescutti et al. 2012). There are only two useful P I lines in the *UV* and two in the *z* band. The near-*IR* P I lines located in the *H* band, 15711.5 and 16482.9 Å (Figure 9) are weak but our high-S/N data yield detections. We estimated P abundances around solar for our RHB stars.

K is produced mainly by oxygen burning and its production rate during nucleosynthesis is still under debate. For example, according to Timmes et al. (1995) [K/Fe] ratios decrease towards lower metallicities, while Samland (1998) and Goswami & Prantzos (2000) suggest [K/Fe] decline in the disk and super solar ratios in halo stars. There are observational studies that favor the theoretical predictions of Samland (1998) and Goswami & Prantzos (2000), e.g., Gratton & Sneden (1987); Chen et al. (2000); Takeda et al. (2002); Zhang et al. (2006); Takeda et al. (2009); Mucciarelli et al. (2017). However, the analytical difficulties of the K I resonance lines render them problematical to map the behavior of K in the Galaxy. The *H* band spectral region provides two more K I lines (Figure 9). Recently, Hawkins et al. (2016) investigated more than 20 elements using a massive Galactic sample from APOGEE data, including [K/Fe]-[Fe/H] relation for $-1.0 \lesssim [\text{Fe}/\text{H}] < 0.5$ (Figure 16 in Hawkins et al.). Their result also supports the predictions of Samland and Goswami & Prantzos. With higher IGRINS *H* band resolution, we were able to study 15163.1 and 15168.4 Å K I lines in more detail. The K abundances we derived from these lines are around solar in our stars.

Our IGRINS abundance analysis of Fe-group elements Sc, Ti, Cr, Co and Ni has been highlighted by consideration of the substantial isotopic substructure of *IR* Ti I lines. Accounting for the isotopic effects yields good agreement with observed Ti I line profiles in the Sun, Arcturus, and our three RHB stars. The general agreement between optical and *IR* abundances for the Fe-peak elements is good with the exception of Sc. Unfortunately, the optical and *IR* Sc abundances are based on different species of this element and the cause of the small (~ 0.15 dex) offset between the Sc abundances in the two wavelength regions cannot be traced easily.

The presence of *n*-capture elements in the near-*IR* were previously discussed by e.g. Hawkins et al. (2016); Haselquist et al. (2016); Cunha et al. (2017). We determined the abundances of three *n*-capture elements in the near-*IR*, all located in the *H* band. Among them, Yb is important because its optical counterpart at 3694 Å falls into a very crowded and low-flux spectral region. We derived near-solar abundances for Yb. The Ce and Nd abundances from both wavelength regions show substantial star-to-star scatter, and needs further investigation.

We computed the CNO abundances using CO, CN and OH molecular features that are present in the near-*IR* at considerable amounts. Our mildly metal-poor stars are relatively hot for OH molecular lines to survive; we could only

detect five useful ones in our RHB stars. The *IR* O abundances are in good agreement with their optical counterparts that were obtained from the forbidden [O I] at 6300 and 6363 Å. The C abundances from *K* band CO lines agree well with the C abundances derived from the CH and C₂ molecular lines in the optical. Finally, we used CN molecular lines in the *H* band to determine N abundances. These results are in good accord with ones obtained from optical CN features.

We also measured the C abundances from seven high-excitation potential C I lines: three in the optical, and four in the near-*IR*. As is seen in Table 8, on average the near-*IR* high-excitation C I lines yield C abundances in reasonable agreement with the ones obtained from their optical counterparts. The mean C abundance from all species in all stars has small internal scatter, $\sigma \leq 0.10$ dex, and these means are always within 0.02 dex with those obtained just from the CO lines. Since CH, C₂, C I, and CO species have different sensitivities to adopted T_{eff} , $\log g$, and O abundance values, their reasonable agreement in our three program stars suggests that the derived mean C abundances are robust. However, this assumption is only based on five stars (including Arcturus and the Sun). Clearly, further investigation is needed with a larger sample to clarify this issue. To the best of our knowledge, this study is the first among others that investigates the C abundances in a more complementary way using four different C features from the optical and near-*IR* wavelength regions.

CNO abundances are the most important indicators of internal nucleosynthesis and envelope mixing in evolved stars. Convective envelope mixing brings up the CN-cycle nuclear processed material to the stellar surface. As a result, C abundance drops, as the N abundance increases (e.g. [Iben 1964, 1967a,b](#)). One of the most important indicators of the convective mixing is the carbon isotopic ratio: $^{12}\text{C}/^{13}\text{C}$. It decreases from its solar value, ~ 90 , to ~ 20 – 30 during the giant branch evolution (e.g. [Charbonnel 1994](#); [Charbonnel et al. 1998](#); [Gratton et al. 2000](#)), sometimes even approaching the CN-cycle equilibrium value of $^{12}\text{C}/^{13}\text{C} = 3$ – 4 (e.g. [Caughlan 1965](#); [Snedden et al. 1986](#); [Cottrell & Sneden 1986](#); [Gratton et al. 2000](#)). Determination of the $^{12}\text{C}/^{13}\text{C}$ ratio in the optical is usually possible from the triplet of ^{13}CN lines near 8004.7 Å. It is the only reliable feature in the optical region and often really weak. IGRINS *K* band has two $\Delta v = 2$ transitions of the ^{12}CO first overtone band heads: (2–0) and (3–1). The ^{13}CO (2–0) and ^{13}CO (3–1) band heads that accompany ^{12}CO are located near 23440 and 23730 Å, respectively. We used both of these regions and re-determined the $^{12}\text{C}/^{13}\text{C}$ ratios for our stars: 12, 8.5 and 15.5 for HIP 54048, HIP 57748 and HIP 114809, respectively (Table 10).

The mean C and N abundances from the optical and near-*IR* for our stars are: $[\text{C}/\text{Fe}] = -0.57$, $[\text{N}/\text{Fe}] = +0.80$ for HIP 54048; $[\text{C}/\text{Fe}] = -0.18$, $[\text{N}/\text{Fe}] = +0.39$ for HIP 57748; and $[\text{C}/\text{Fe}] = -0.31$, $[\text{N}/\text{Fe}] = +0.58$ for HIP 114809. The mean O abundances are within ± 0.1 dex in HIP 54048 and HIP 57748, and slightly above solar, $[\text{O}/\text{Fe}] = 0.13$ dex, in HIP 114809. The C abundance is considerably low while the N abundance is substantially high in HIP 54048 compared to other RHB stars. In fact the $[\text{C}/\text{N}] = -1.37$ of HIP 54048 puts its location beyond the $[\text{C}/\text{N}]$ limits recently studied by, e.g., [Lagarde et al. \(2017, 2018\)](#), which might imply a very high initial mass for this star. Further investigation is needed for HIP 54048. The $[\text{C}/\text{N}]$ values for HIP 57748 and HIP 114809 are -0.57 and -0.89 , respectively. These values also indicates high initial masses according to [Lagarde et al. \(2017\)](#) and [Lagarde et al. \(2018\)](#). In all three cases a thermohaline mixing process is required in order to explain the low $^{12}\text{C}/^{13}\text{C}$ ratios observed in our stars (Table 10).

Near-*IR* IGRINS high-resolution spectra provide an important new opportunity to study stellar chemical compositions in detail. As discussed above, *H* and *K* bands often yield more reliable abundance results, while providing new features that come with open questions. Our next paper with about 70 RHB stars will explore the issues that need further investigation with a larger sample and provide more realistic statistical results for many elements in the near-*IR* spectral range.

We like to thank Nils Ryde, Brian Thorsbro and Elisabetta Caffau for helpful discussions. Our work has been supported by The Scientific and Technological Research Council of Turkey (TÜBİTAK, project No. 112T929), by the US National Science Foundation grants AST 1211585 and AST 1616040, and by the University of Texas Rex G. Baker, Jr. Centennial Research Endowment. This research has made use of the SIMBAD database, operated at CDS, Strasbourg, France. One of the authors (JEL) is supported by the NSF under Grant AST-1516182. This work used the Immersion Grating Infrared Spectrometer (IGRINS) that was developed under a collaboration between the University of Texas at Austin and the Korea Astronomy and Space Science Institute (KASI) with the financial support of the US National Science Foundation under grant AST-1229522, of the University of Texas at Austin, and of the Korean GMT Project of KASI.

Software: IRAF ([Tody 1993](#) and references therein), MOOG ([Snedden 1973](#)), ATLAS ([Kurucz 2011](#))

REFERENCES

- Afşar, M., Bozkurt, Z., Böcek Topcu, G., et al. 2018a, *AJ*, 155, 240, (Afşar18a)
- Afşar, M., Bozkurt, Z., Böcek Topcu, G., & Sneden, C. 2018b, *in preparation*
- Afşar, M., Sneden, C., & For, B.-Q. 2012, *AJ*, 144, 20, (ASF12)
- Afşar, M., Sneden, C., Frebel, A., et al. 2016, *ApJ*, 819, 103, (Afşar16)
- Anastassov, A., Gangrsky, Y. P., Marinova, K. P., Markov, B. N., & Zemlyanoi, S. G. 1994, *Zeitschrift fur Physik D Atoms Molecules Clusters*, 30, 275
- Asplund, M., Grevesse, N., Sauval, A. J., & Scott, P. 2009, *ARA&A*, 47, 481
- Azaroual, E. M., Luc, P., & Vetter, R. 1992, *Zeitschrift fur Physik D Atoms Molecules Clusters*, 24, 161
- Barbuy, B., Zoccali, M., Ortolani, S., et al. 2007, *AJ*, 134, 1613
- Barklem, P. S., & Asplund-Johansson, J. 2005, *A&A*, 435, 373
- Barklem, P. S., Piskunov, N., & O'Mara, B. J. 2000, *A&AS*, 142, 467
- Blackwell-Whitehead, R. J., Lundberg, H., Nave, G., et al. 2006, *MNRAS*, 373, 1603
- Böcek Topcu, G., Afşar, M., Schaeuble, M., & Sneden, C. 2015, *MNRAS*, 446, 3562
- Böcek Topcu, G., Afşar, M., & Sneden, C. 2016, *MNRAS*, 463, 580
- Caffau, E., Bonifacio, P., Faraggiana, R., et al. 2005, *A&A*, 441, 533
- Caffau, E., Bonifacio, P., Faraggiana, R., & Steffen, M. 2011, *A&A*, 532, A98
- Caffau, E., Ludwig, H.-G., Bonifacio, P., et al. 2010, *A&A*, 514, A92
- Carrera, R., & Pancino, E. 2011, *A&A*, 535, A30
- Caughlan, G. R. 1965, *ApJ*, 141, 688
- Cescutti, G., Matteucci, F., Caffau, E., & François, P. 2012, *A&A*, 540, A33
- Charbonnel, C. 1994, *A&A*, 282, 811
- Charbonnel, C., Brown, J. A., & Wallerstein, G. 1998, *A&A*, 332, 204
- Chen, Y. Q., Nissen, P. E., Zhao, G., Zhang, H. W., & Benoni, T. 2000, *A&AS*, 141, 491
- Cohen, J. G., Christlieb, N., McWilliam, A., et al. 2004, *ApJ*, 612, 1107
- Cottrell, P. L., & Sneden, C. 1986, *A&A*, 161, 314
- Cunha, K., Smith, V. V., Hasselquist, S., et al. 2017, *ApJ*, 844, 145
- Den Hartog, E. A., Lawler, J. E., Sneden, C., & Cowan, J. J. 2003, *ApJS*, 148, 543
- For, B.-Q., & Sneden, C. 2010, *AJ*, 140, 1694
- Fukue, K., Matsunaga, N., Yamamoto, R., et al. 2015, *ApJ*, 812, 64
- Furmann, B., Stefańska, D., Krzykowski, A., Jarosz, A., & Kajoch, A. 1996, *Zeitschrift fur Physik D Atoms Molecules Clusters*, 37, 289
- Gaia Collaboration, Brown, A. G. A., Vallenari, A., et al. 2018, *ArXiv e-prints*, arXiv:1804.09365
- Gaia Collaboration, Prusti, T., de Bruijne, J. H. J., et al. 2016, *A&A*, 595, A1
- Gangrsky, Y. P., Marinova, K. P., & Zemlyanoi, S. G. 1995, *Journal of Physics B Atomic Molecular Physics*, 28, 957
- Girardi, L. 1999, *MNRAS*, 308, 818
- Girardi, L., Groenewegen, M. A. T., Weiss, A., & Salaris, M. 1998, *MNRAS*, 301, 149
- Goswami, A., & Prantzos, N. 2000, *A&A*, 359, 191
- Gratton, R. G., & Sneden, C. 1987, *A&A*, 178, 179
- Gratton, R. G., Sneden, C., Carretta, E., & Bragaglia, A. 2000, *A&A*, 354, 169
- Hamdani, S., North, P., Mowlavi, N., Raboud, D., & Mermilliod, J.-C. 2000, *A&A*, 360, 509
- Hasselquist, S., Shetrone, M., Cunha, K., et al. 2016, *ApJ*, 833, 81
- Hawkins, K., Masseron, T., Jofré, P., et al. 2016, *A&A*, 594, A43
- Hinkle, K., Wallace, L., & Livingston, W. C. 1995, *Infrared atlas of the Arcturus spectrum, 0.9-5.3 microns* (Ast. Soc. Pacific, San Francisco, Calif.)
- Iben, Jr., I. 1964, *ApJ*, 140, 1631
- . 1967a, *ApJ*, 147, 650
- . 1967b, *ApJ*, 147, 624
- Ishigaki, M. N., Chiba, M., & Aoki, W. 2012, *ApJ*, 753, 64
- Ivans, I. L., Simmerer, J., Sneden, C., et al. 2006, *ApJ*, 645, 613
- Jacobson, H. R., Friel, E. D., & Pilachowski, C. A. 2007, *AJ*, 134, 1216
- Jacobson, H. R., Thanathibodee, T., Frebel, A., et al. 2014, *ApJL*, 796, L24
- Jin, W.-G., Nemoto, Y., & Minowa, T. 2009, *Journal of the Physical Society of Japan*, 78, 094301
- Kaempf, T. A., de Boer, K. S., & Altmann, M. 2005, *A&A*, 432, 879
- Kobayashi, C., Umeda, H., Nomoto, K., Tominaga, N., & Ohkubo, T. 2006, *ApJ*, 653, 1145
- Korotin, S. A. 2009, *Astronomy Reports*, 53, 651
- Kraft, R. P. 1994, *PASP*, 106, 553
- Kramida, A., Ralchanko, Y., Reader, J., & NIST ASD Team. 2014, *NIST Atomic Spectra Database (version 5.2)*
- Kurucz, R. L. 2011, *Canadian Journal of Physics*, 89, 417
- Lagarde, N., Robin, A. C., Reylé, C., & Nasello, G. 2017, *A&A*, 601, A27
- Lagarde, N., Reylé, C., Robin, A. C., et al. 2018, *ArXiv e-prints*, arXiv:1806.01868
- Lawler, J. E., & Dakin, J. T. 1989, *Journal of the Optical Society of America B Optical Physics*, 6, 1457
- Lawler, J. E., Guzman, A., Wood, M. P., Sneden, C., & Cowan, J. J. 2013, *ApJS*, 205, 11
- Lawler, J. E., Sneden, C., & Cowan, J. J. 2015, *ApJS*, 220, 13
- Lawler, J. E., Sneden, C., Cowan, J. J., Ivans, I. I., & Den Hartog, E. A. 2009, *ApJS*, 182, 51
- Lind, K., Asplund, M., Barklem, P. S., & Belyaev, A. K. 2011, *A&A*, 528, A103
- Lobel, A. 2011, *Canadian Journal of Physics*, 89, 395
- Lodders, K., & Amari, S. 2005, *Chemie der Erde / Geochemistry*, 65, 93
- Luc, P., & Vetter, R. 1996, *Zeitschrift fur Physik D Atoms Molecules Clusters*, 37, 255
- Luc, P., Vetter, R., Bauche-Arnoult, C., & Bauche, J. 1994, *Zeitschrift fur Physik D Atoms Molecules Clusters*, 31, 145
- Maas, Z. G., Pilachowski, C. A., & Cescutti, G. 2017, *ApJ*, 841, 108
- Majewski, S. R., APOGEE Team, & APOGEE-2 Team. 2016, *Astronomische Nachrichten*, 337, 863
- Majewski, S. R., Schiavon, R. P., Frinchaboy, P. M., et al. 2017, *AJ*, 154, 94
- Mucciarelli, A., Merle, T., & Bellazzini, M. 2017, *A&A*, 600, A104
- Nordlander, T., & Lind, K. 2017, *A&A*, 607, A75
- Park, C., Jaffe, D. T., Yuk, I.-S., et al. 2014, *in Society of Photo-Optical Instrumentation Engineers (SPIE) Conference Series, Vol. 9147, Society of Photo-Optical Instrumentation Engineers (SPIE) Conference Series*, 1
- Pehlivan, A., Nilsson, H., & Hartman, H. 2015, *A&A*, 582, A98
- Ramírez, I., & Allende Prieto, C. 2011, *ApJ*, 743, 135
- Reddy, A. B. S., Giridhar, S., & Lambert, D. L. 2012, *MNRAS*, 419, 1350
- Rich, R. M., Sosin, C., Djorgovski, S. G., et al. 1997, *ApJL*, 484, L25

- Roederer, I. U., Jacobson, H. R., Thanathibodee, T., Frebel, A., & Toller, E. 2014, *ApJ*, 797, 69
- Ryabchikova, T., Piskunov, N., Kurucz, R. L., et al. 2015, *Phys. Scr.*, 90, 054005
- Samland, M. 1998, *ApJ*, 496, 155
- Shetrone, M., Bizyaev, D., Lawler, J. E., et al. 2015, *ApJS*, 221, 24
- Smith, G. 1981, *A&A*, 103, 351
- Smith, G., & Raggett, D. S. J. 1981, *Journal of Physics B Atomic Molecular Physics*, 14, 4015
- Sneden, C. 1973, *ApJ*, 184, 839
- Sneden, C., Lucatello, S., Ram, R. S., Brooke, J. S. A., & Bernath, P. 2014, *ApJS*, 214, 26
- Sneden, C., Pilachowski, C. A., & Vandenberg, D. A. 1986, *ApJ*, 311, 826
- Sobeck, J. S., Lawler, J. E., & Sneden, C. 2007, *ApJ*, 667, 1267
- Sobeck, J. S., Kraft, R. P., Sneden, C., et al. 2011, *AJ*, 141, 175
- Takeda, Y., Kaneko, H., Matsumoto, N., et al. 2009, *PASJ*, 61, 563
- Takeda, Y., Omiya, M., Harakawa, H., & Sato, B. 2016, *PASJ*, 68, 81
- Takeda, Y., Zhao, G., Chen, Y.-Q., Qiu, H.-M., & Takada-Hidai, M. 2002, *PASJ*, 54, 275
- Takeda, Y., Zhao, G., Takada-Hidai, M., et al. 2003, *Chinese J. Astron. Astrophys.*, 3, 316
- Tautvaišienė, G. 1996, *Astronomische Nachrichten*, 317, 29
- . 1997, *MNRAS*, 286, 948
- Tautvaišienė, G., Edvardsson, B., Tuominen, I., & Ilyin, I. 2001, *A&A*, 380, 578
- Timmes, F. X., Woosley, S. E., & Weaver, T. A. 1995, *ApJS*, 98, 617
- Tody, D. 1993, in *Astronomical Society of the Pacific Conference Series*, Vol. 52, *Astronomical Data Analysis Software and Systems II*, ed. R. J. Hanisch, R. J. V. Brissenden, & J. Barnes, 173
- Truran, J. W. 1973, *Space Sci. Rev.*, 15, 23
- Unsöld, A. 1955, *Physik der Sternatmosphären*, MIT besonderer Berücksichtigung der Sonne.
- van Deelen, F. 2017, *Hyperfine structure measurements in scandium for IR spectroscopy*, Lund University Student Paper
- van Leeuwen, F. 2007, *A&A*, 474, 653
- Wallace, L., & Livingston, W. 2003, *An atlas of the solar spectrum in the infrared from 1850 to 9000 cm⁻¹ (1.1 to 5.4 micrometer)* (Tucson: National Solar Observatory, National Optical Astronomy Observatory, NSO Technical Report)
- Wallerstein, G., & Helfer, H. L. 1959, *ApJ*, 129, 720
- Wiese, W. L., & Martin, G. A. 1980, *Wavelengths and transition probabilities for atoms and atomic ions: Part 2. Transition probabilities* (NSRDS-NBS Vol. 68)
- Wood, M. P., Lawler, J. E., & Shetrone, M. D. 2014, *ApJL*, 787, L16
- Wood, M. P., Lawler, J. E., Sneden, C., & Cowan, J. J. 2013, *ApJS*, 208, 27
- . 2014b, *ApJS*, 211, 20
- Yuk, I.-S., Jaffe, D. T., Barnes, S., et al. 2010, in *Society of Photo-Optical Instrumentation Engineers (SPIE) Conference Series*, Vol. 7735, *Society of Photo-Optical Instrumentation Engineers (SPIE) Conference Series*, 1
- Zhang, H. W., Gehren, T., Butler, K., Shi, J. R., & Zhao, G. 2006, *A&A*, 457, 645

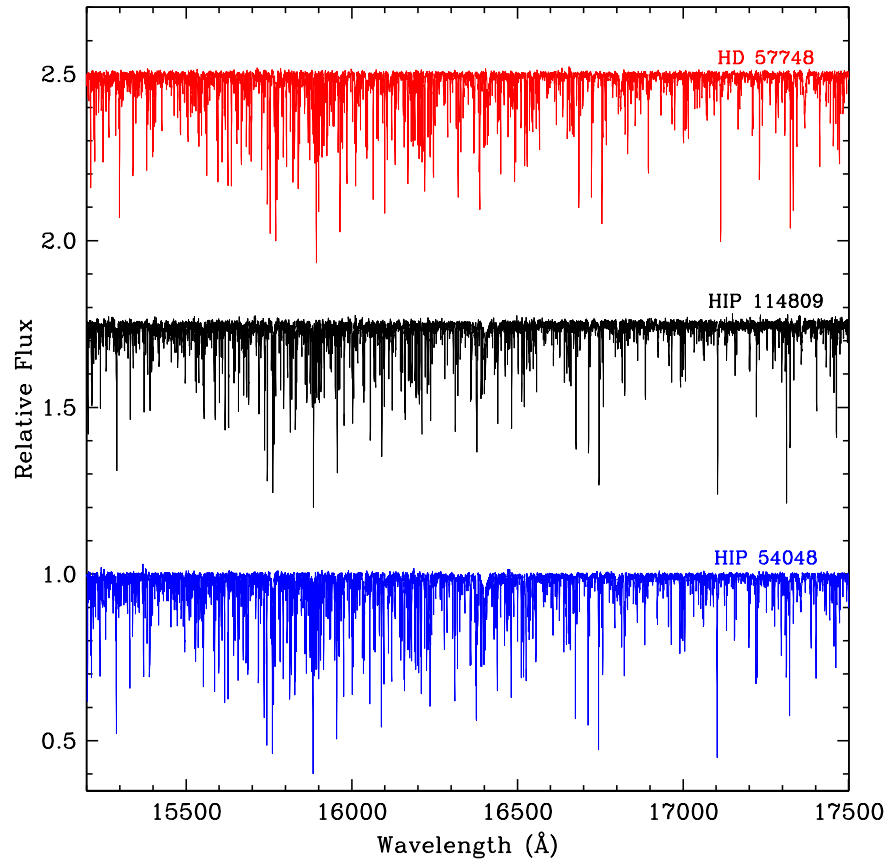


Figure 1. IGRINS H band spectra of three RHB stars in air wavelengths: HIP 57748 (red), HIP 114809 (black), and HIP 54048 (blue). For plotting clarity, we shifted the relative flux scale of HIP 57748 and HIP 114809 vertically with additive constants. The low and high wavelength edges of the spectra have been trimmed to avoid the edges with severe telluric contamination.

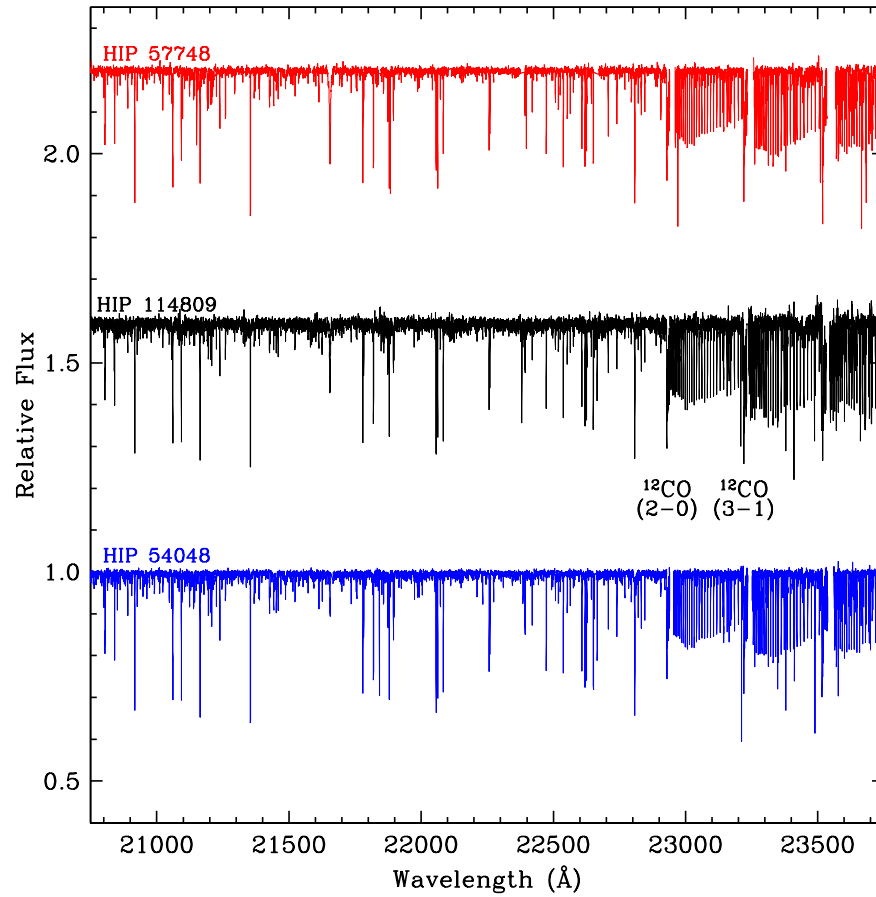


Figure 2. IGRINS *K* band spectra of three RHB stars in air wavelengths: HIP 57748 (red), HIP 114809 (black), and HIP 54048 (blue). The loci of the ^{12}CO (2-0) and ^{12}CO (3-1) band heads are also shown.

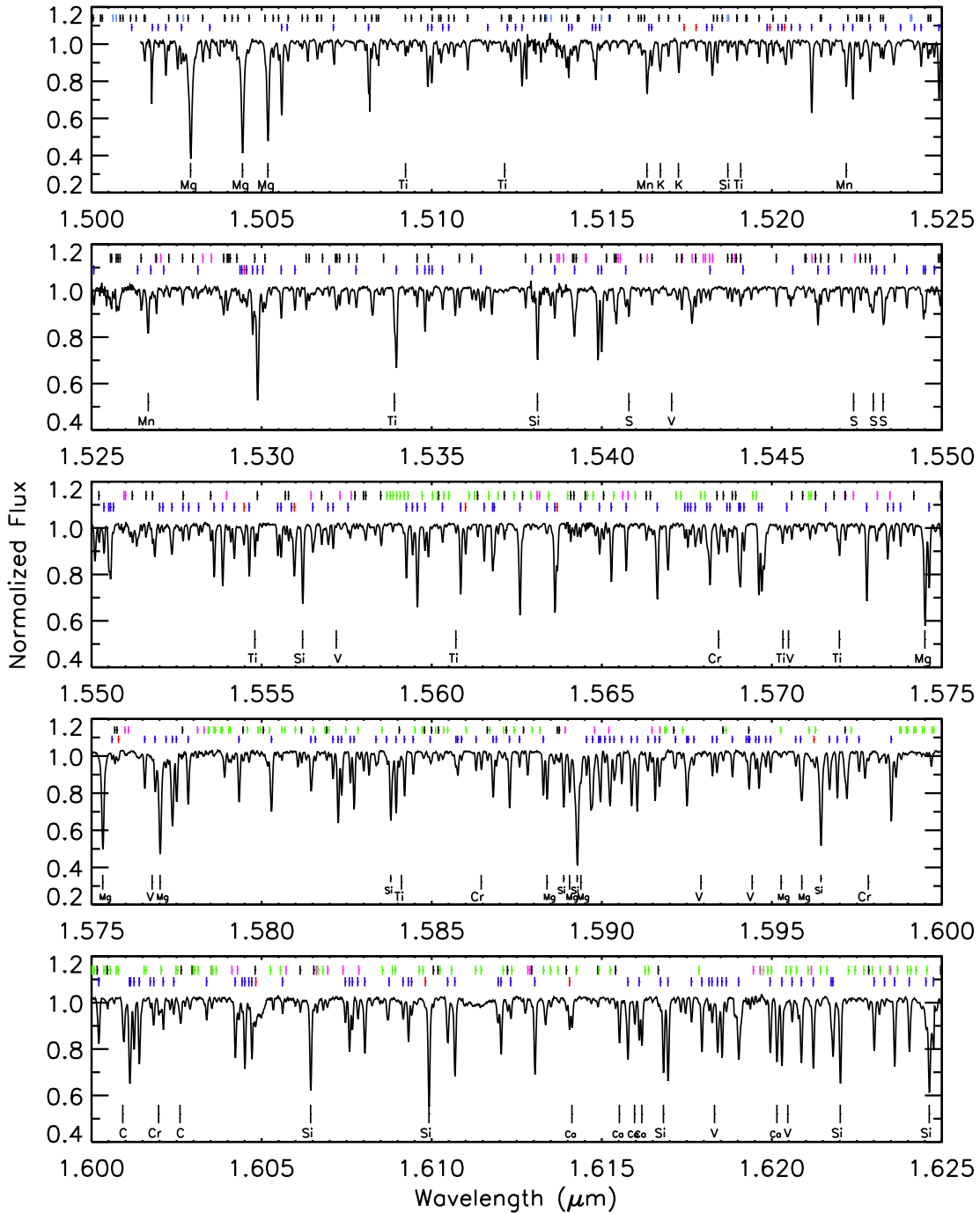


Figure 3. A portion of the *H* and *K* band spectral atlas for our stars is presented. We use the HIP 54048 spectrum as the benchmark of RHB stars. In this figure the atomic lines are labeled with their names, including substantial amount of Fe and Ni, which are indicated with blue and red ticks, respectively, on the top second row of the figure panel. CN, OH and CO molecular features are illustrated with black, magenta and green ticks, respectively, on the top row of the figure panel. All line identifications are vacuum wavelengths (Hinkle et al. 1995). The IGRINS spectrum has been shifted to the reference frame of the line lists.

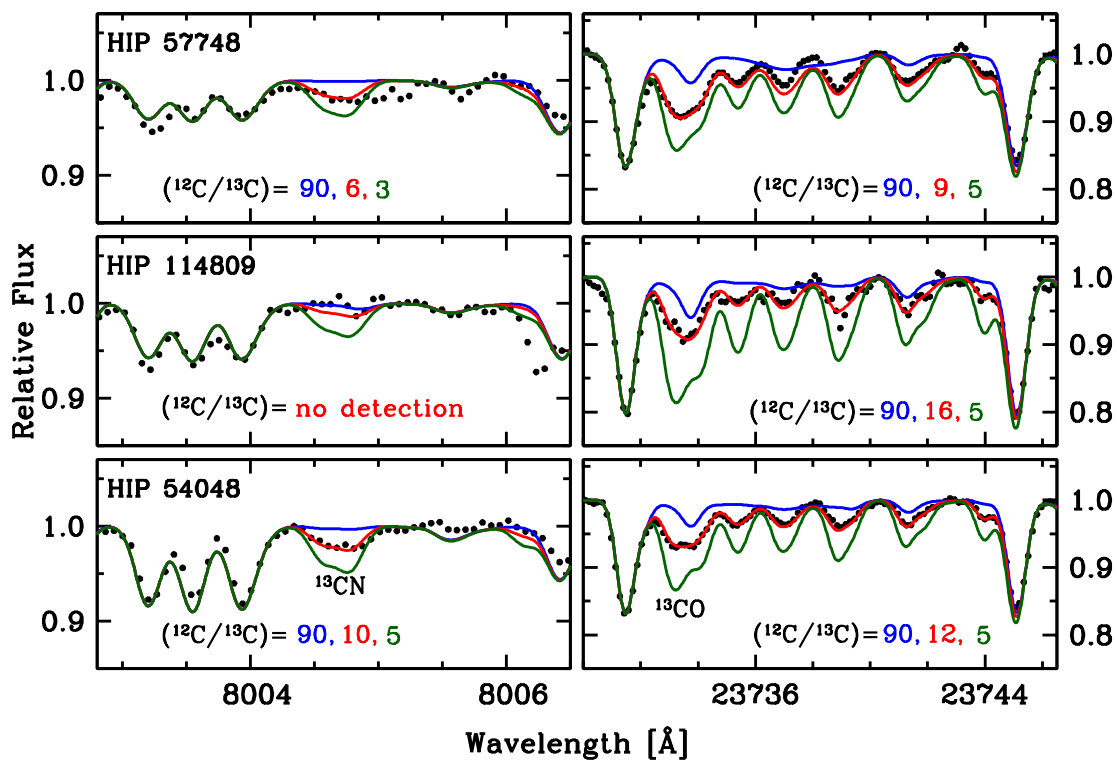


Figure 4. ^{13}CN at 8004.7 Å and ^{13}CO (3-1) band head in the K band are shown for our targets. Observed spectra are given in black dots. Blue (top), red (middle) and green (bottom) lines represent the synthetic spectra for assumed $^{12}\text{C}/^{13}\text{C}$ ratios. The red line is the best matching synthesis to the observed spectrum. Assumed $^{12}\text{C}/^{13}\text{C}$ ratios are also given in the figure panels.

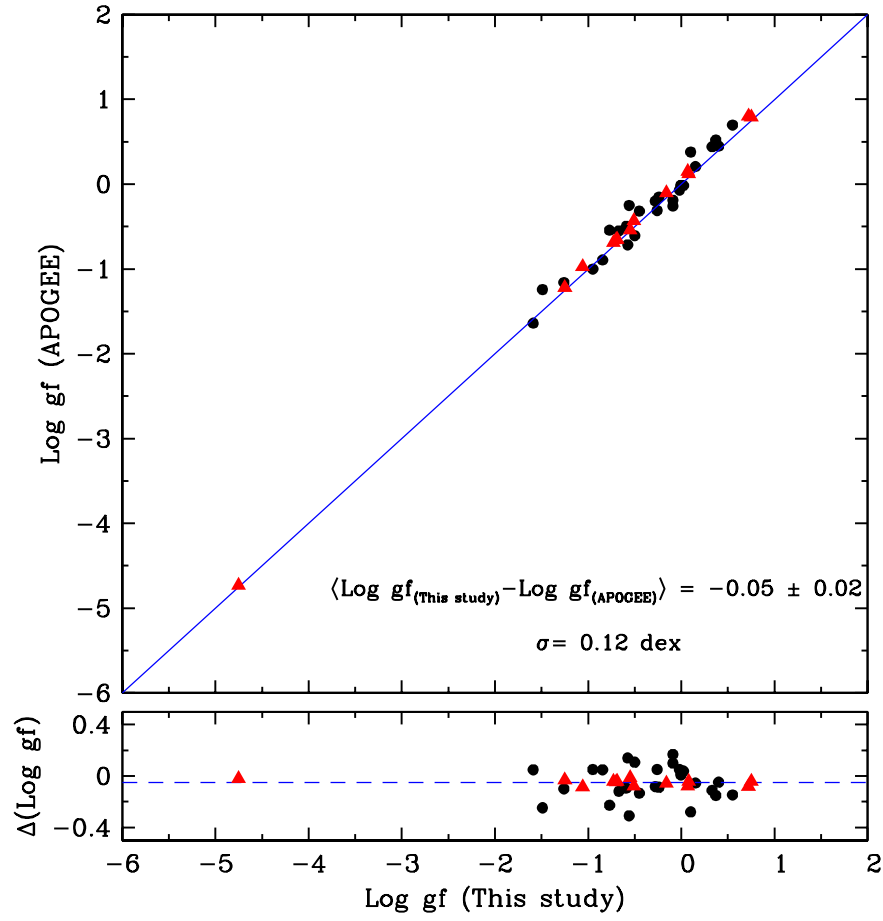


Figure 5. Comparison of $\log gf$ values (This study vs. APOGEE) of nine different elements (see §4.1) are plotted in the top panel. Red triangles represent the $\log gf$ values of Fe I lines. Bottom panel shows the $\Delta(\log gf) = \log gf_{(\text{This study})} - \log gf_{(\text{APOGEE})}$. In the top panel, the blue line denotes equality of the $\log gf$ values. The blue dashed line in the bottom panel denotes the mean of the differences.

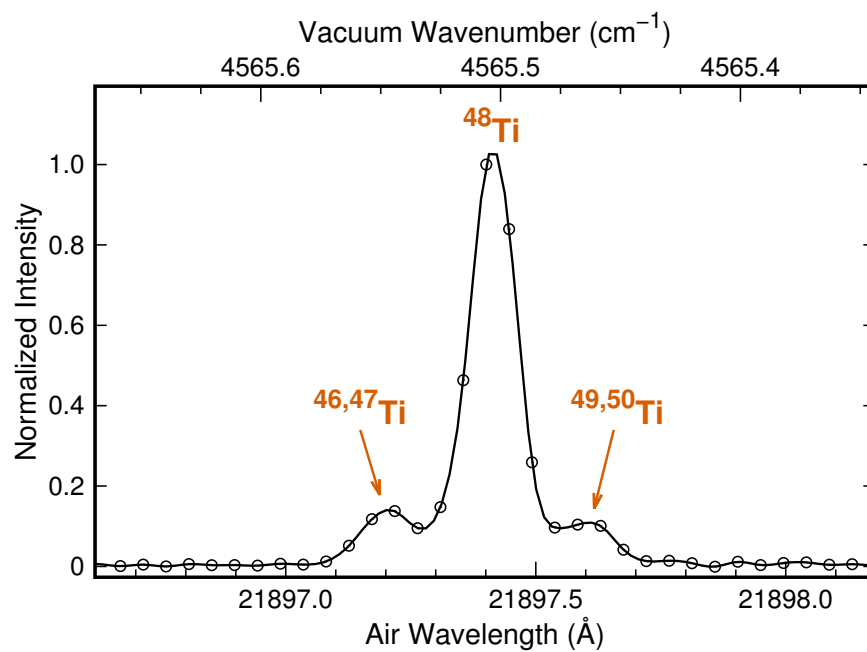


Figure 6. Example laboratory spectrum for one of the Ti I IR lines included in this study. The main component of the line is the dominant ^{48}Ti isotope, while the side peaks correspond to the minor Ti isotopes. This spectrum was recorded using the NIST 2-m FTS and a high-current hollow cathode lamp, and is representative of the type used to derive our Ti I isotope shifts.

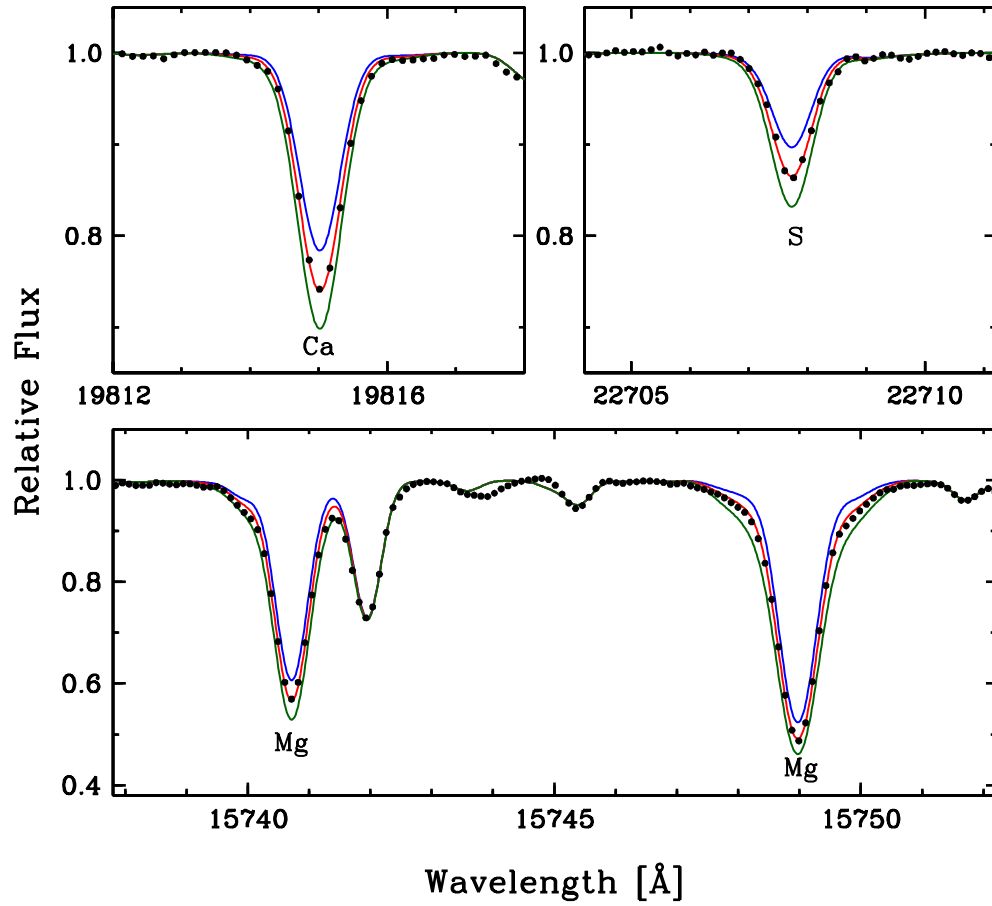


Figure 7. Example regions for Mg, Ca and S in HIP 54048. The syntheses represented with blue and green lines depart from the best fit (red line) by ± 0.3 dex. The lines, colors and symbols are the same as in Figure 4.

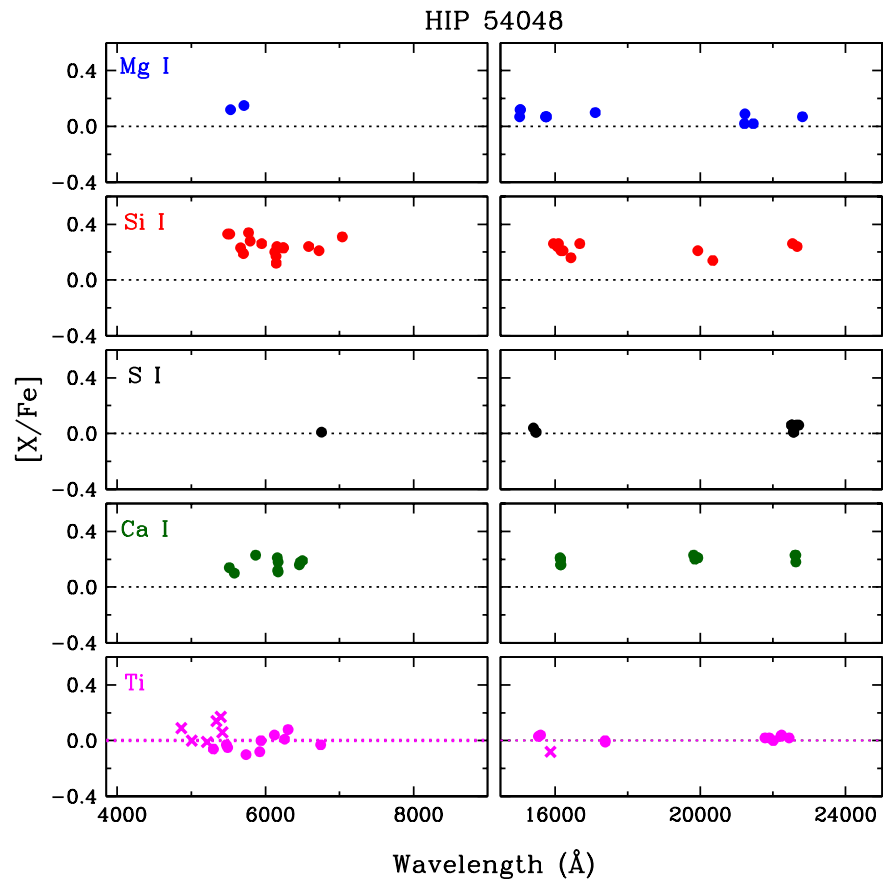


Figure 8. Relative abundance ratios $[X/Fe]$ of α elements in HIP 54048. Ti panel includes both Ti I (dots) and Ti II (crosses). We included Ti in this plot since it is sometimes regarded as an α element.

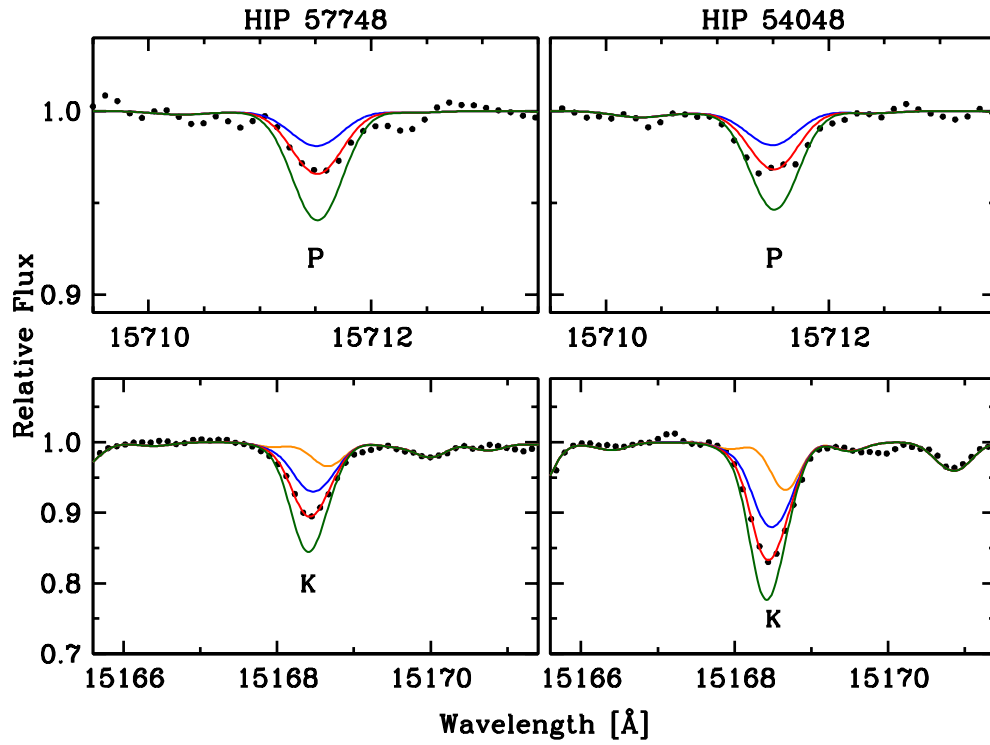


Figure 9. One of the P and K regions in HIP 54048 and HIP 57748 illustrated as an example. The syntheses illustrated with blue and green lines depart from the best fit (red line) by ± 0.3 dex. K lines are mainly blend with CN features. Orange lines assume “no K detection” to draw attention to the effect of the blended feature. The lines, colors and symbols are the same as in Figure 4.

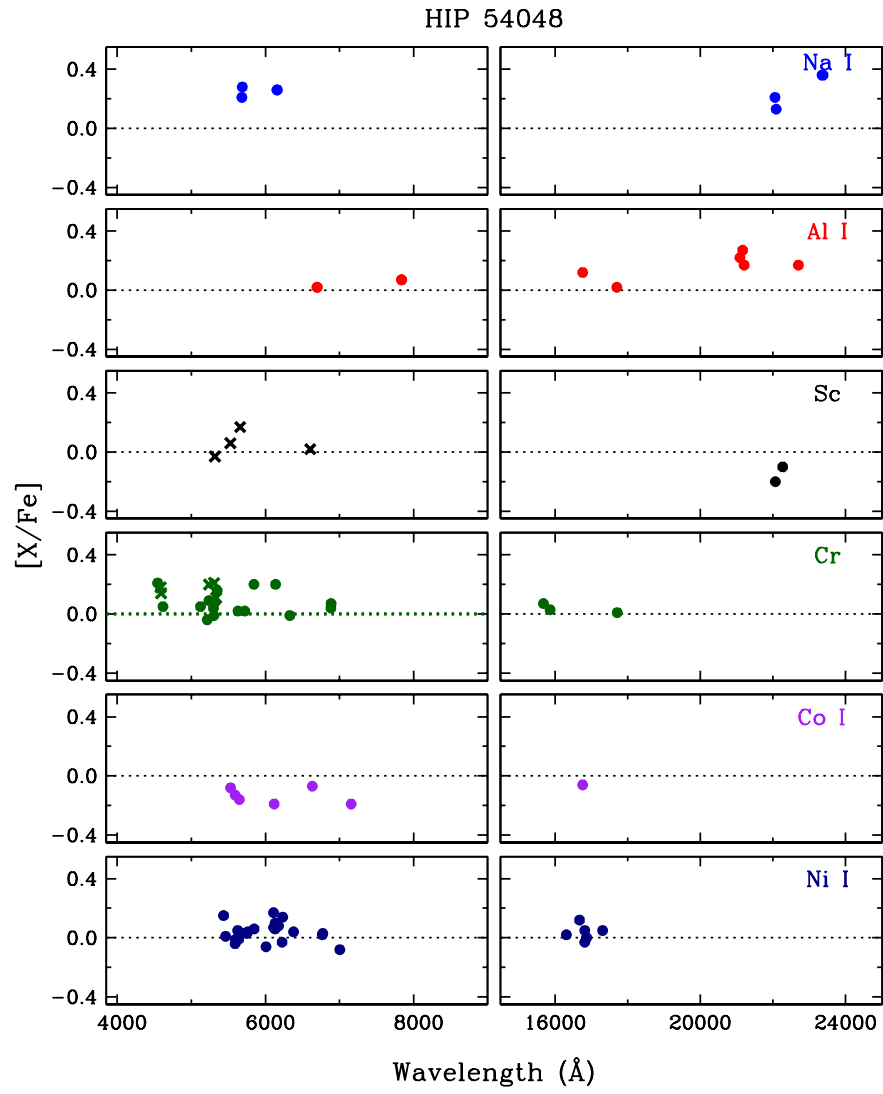


Figure 10. Relative abundance ratios $[X/Fe]$ of other elements in HIP 54048. Sc and Cr panels include both neutral (dots) and ionized (crosses) species of the same element.

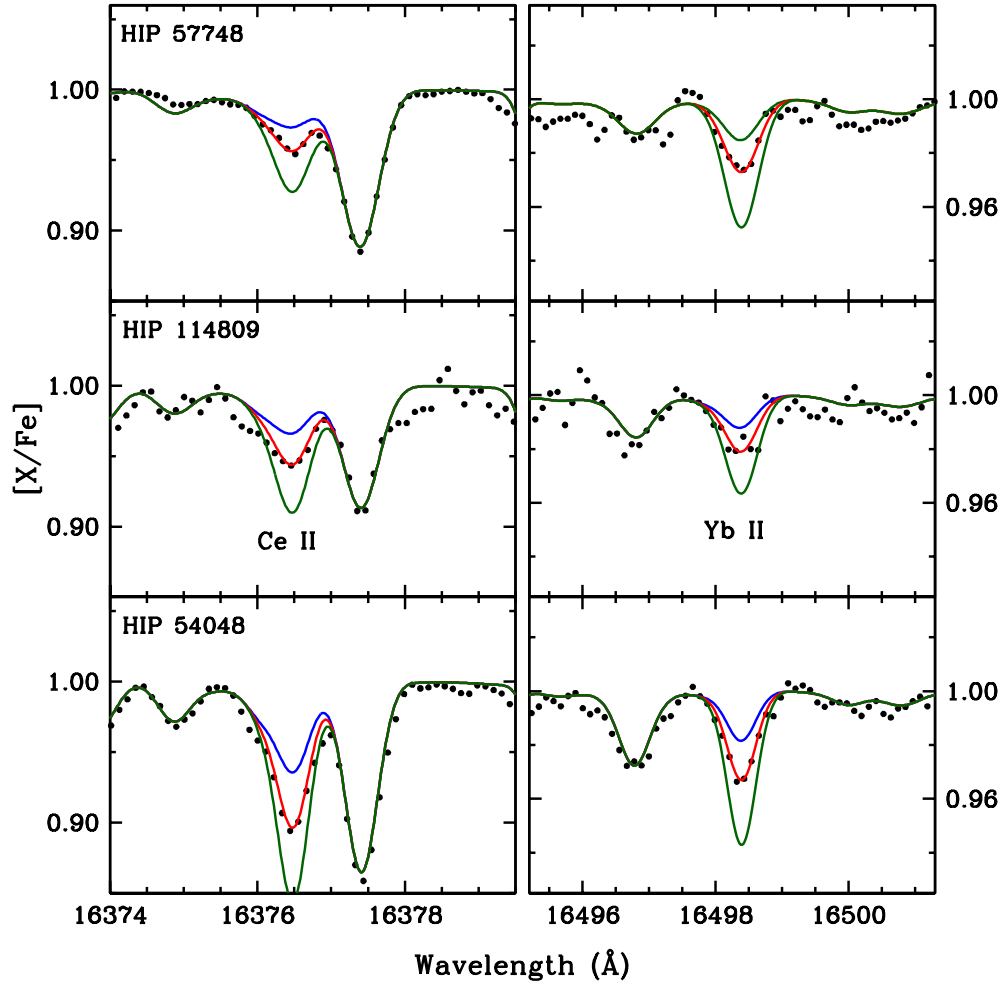


Figure 11. Neutron capture elements Ce II (left panel) and Yb II (right panel) detected in our stars. The syntheses illustrated with blue and green lines depart from the best fit (red line) by ± 0.3 dex. The lines, colors and symbols are the same as in Figure 4.

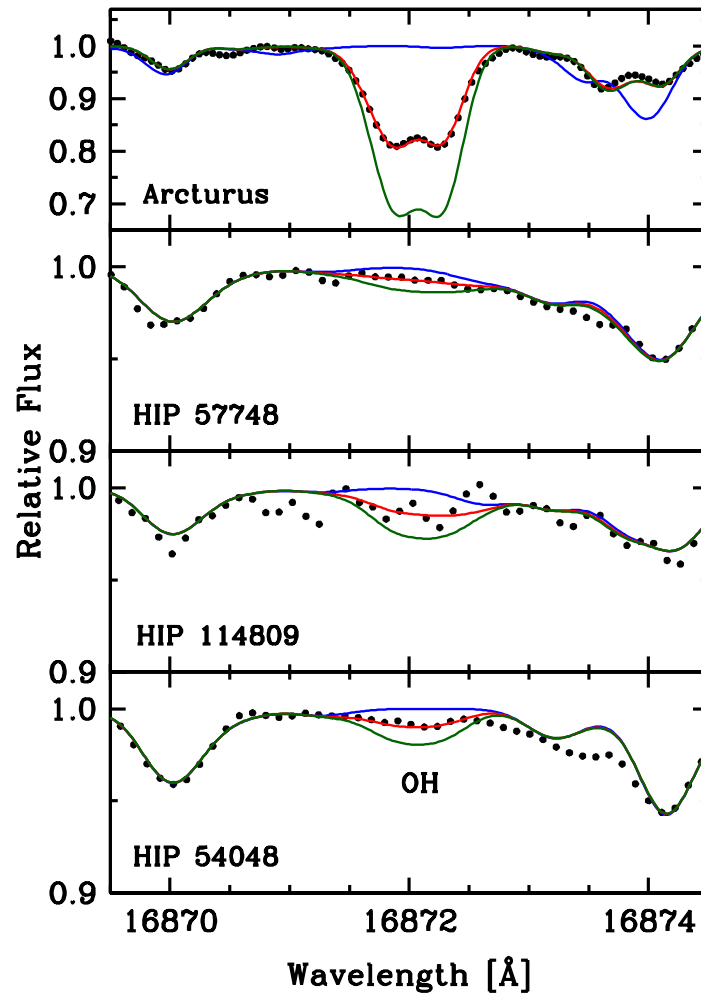


Figure 12. OH line at 16872 Å in all RHB stars. Since the OH lines are considerably weak in all RHB stars, the syntheses shown with blue lines are assumed to be no OH detection. The syntheses illustrated with green line depart from the best fit (red line) by +0.3 dex. The lines, colors and symbols are the same as in Figure 4.

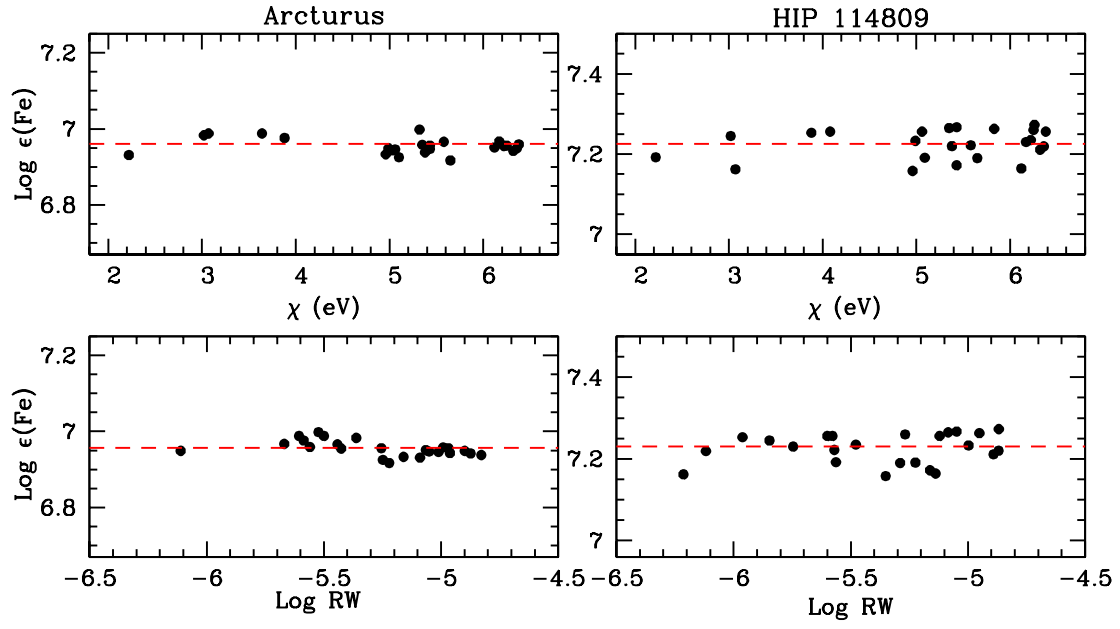


Figure 13. Testing the EW measurements of Fe I lines located in the H and K bands by setting the model atmosphere parameters obtained from the optical lines (§3). Top panel shows the line abundances plotted as a function of the excitation potential χ (eV), and the bottom panel as a function of the reduced width RW.

Table 1. Basic Program Star Data

Star	Other	V^a	H^a	K^a	π_{Hip}^b mas	π_{Gaia}^c mas	M_V^d	Date (UT) ^e (2014)	Exposure (s)	S/N
HIP 54048	HD 95870	6.34	4.45	4.32	6.04	5.84	0.18	May 24	480	~450
HIP 57748	HD 102857	7.90	6.12	6.01	4.47	4.77	1.29	May 27	720	~400
HIP 114809	HD 219418	6.81	4.88	4.76	6.22	4.78	0.21	October 19	120	~200

^aSIMBAD database

^b[van Leeuwen \(2007\)](#)

^cFrom GAIA DR2 ([Gaia Collaboration et al. 2016, 2018](#))

^dBased on GAIA DR2

^eDate of IGRINS observations

Table 2. Model Atmosphere Parameters^a

Star	T_{eff} (K)	$\log g$	[M/H]	ξ_t (km s ⁻¹)
HIP 54048	5099	2.63	-0.16	1.38
HIP 57748	5307	2.34	-0.17	1.82
HIP 114809	5139	2.59	-0.38	1.31

^a[Afşar et al. \(2018a\)](#)

Table 3. Abundances from Individual Transition

Species (X)	λ (Å)	χ (eV)	log gf	source ^a	method ^b	log $\epsilon(X)$		
						HIP 54048	HIP 57748	HIP 114809
C I	5052.149	7.69	-1.30	1	SYN	7.70	8.12	7.75
C I	5380.331	7.69	-1.62	1	SYN	7.77	8.18	7.91
C I	8335.144	7.69	-0.44	1	SYN	7.82	8.35	7.91
C I	16021.700	9.63	0.08	3	SYN	7.73	8.14	7.86
C I	16890.386	9.00	0.42	3	SYN	7.83	8.28	7.94
C I	17455.979	9.69	0.16	3	SYN	7.83	8.24	7.94
C I	21023.131	9.17	-0.40	1	SYN	7.73	8.16	7.84
Na I	5682.633	2.10	-0.71	1	SYN	6.28	6.10	6.27
Na I	5688.194	2.10	-1.41	1	SYN	6.35	6.10	6.27
Na I	6154.226	2.10	-1.56	1	SYN	6.33	6.10	6.20
...								

^aSources for the gf values: 1. [Kramida et al. \(2014\)](#); 2. [Kurucz \(2011\)](#); 3. Revsol: reverse solar analysis; 4. [Lobel \(2011\)](#); 5. [Ryabchikova et al. \(2015\)](#); 6. [Ivans et al. \(2006\)](#); 7. [For & Sneden \(2010\)](#); 8. [Ishigaki et al. \(2012\)](#); 9. [Barbuy et al. \(2007\)](#); 10. [Reddy et al. \(2012\)](#); 11. [Carrera & Pancino \(2011\)](#); 12. [Smith \(1981\)](#), 13. [Hamdani et al. \(2000\)](#); 14. [Smith & Raggatt \(1981\)](#); 15. [Lawler et al. \(2013\)](#); 16. [Wood et al. \(2013\)](#); 17. [Wood et al. \(2014\)](#); 18. [Sobeck et al. \(2007\)](#); 19. [Cohen et al. \(2004\)](#); 20. [Sobeck et al. \(2011\)](#); 21. [Wood et al. \(2014b\)](#); 22. [Jacobson et al. \(2007\)](#); 23. [Wiese & Martin \(1980\)](#); 24. [Lawler et al. \(2009\)](#); 25. [Cunha et al. \(2017\)](#); 26. [Den Hartog et al. \(2003\)](#); 27. [Hasselquist et al. \(2016\)](#); 28. [Lawler & Dakin \(1989\)](#); 29. [Pehlivan et al. \(2015\)](#); 30. [Lawler et al. \(2015\)](#).

^bSYN = spectrum synthesis, EW = equivalent width matching.

NOTE—This table is available in its entirety in a machine-readable form in the online journal.

Table 4. HIP 54048 Mean Abundances

Species	[X/Fe] optical	σ	#	[X/Fe] infrared	σ	#
C ^a	-0.62	0.01	...	-0.53	0.00	...
N ^b	0.79		...	0.81	0.05	...
O ^c	-0.07	0.12	2	-0.06	0.06	8
Na I	0.25	0.03	4	0.27	0.11	4
Mg I	0.14	0.02	2	0.07	0.03	11
Al I	0.05	0.03	4	0.16	0.09	6
Si I	0.24	0.06	16	0.22	0.04	12
P I	0.04	0.00	2
S I	0.01	...	1	0.04	0.02	10
K I	0.61	...	1	0.06	0.10	2
Ca I	0.16	0.04	10	0.20	0.03	11
Sc I	-0.15	0.07	2
Sc II	0.07	0.07	6
Ti I	-0.02	0.05	10	0.02	0.02	10
Ti II	0.07	0.07	6	-0.08	...	1
Cr I	0.07	0.08	16	0.04	0.03	3
Cr II	0.17	0.04	5
Fe I ^d	7.33	0.06	68	7.39	0.04	26
Fe II ^d	7.33	0.05	12
Co I	-0.14	0.05	6	-0.06	...	1
Ni I	0.04	0.06	22	0.04	0.05	6
Ce II	0.16	0.04	4	0.29	0.07	6
Nd II	0.25	0.04	2	0.37	...	1
Yb II	0.13	...	1

^aC abundance: optical from CH, C₂, infrared from CO

^bN abundance: optical and infrared from CN

^cO abundance: optical from [O I], infrared from OH

^dlog ϵ values are given for Fe I and Fe II

Table 5. HIP 57748 Mean Abundances

Species	[X/Fe]	σ optical	#	[X/Fe]	σ infrared	#
C ^a	-0.24	0.06	...	-0.12	0.04	...
N ^b	0.40	0.37	0.02	...
O ^c	-0.07	0.06	2	0.03	0.15	...
Na I	0.03	...	4	-0.05	0.10	4
Mg I	0.18	0.04	2	0.15	0.09	11
Al I	-0.15	0.01	4	-0.06	0.11	6
Si I	0.28	0.07	13	0.26	0.04	11
P I	0.03	0.04	2
S I	0.07	...	1	0.10	0.04	10
K I	0.62	...	1	-0.03	0.00	2
Ca I	0.03	0.05	11	0.05	0.05	11
Sc I
Sc II	-0.22	0.06	5
Ti I	-0.19	0.06	8	-0.10	0.03	9
Ti II	-0.07	0.06	5	-0.24	...	1
Cr I	0.00	0.06	16	-0.01	0.03	3
Cr II	0.16	0.05	4
Fe I ^d	7.33	0.06	67	7.40	0.05	25
Fe II ^d	7.31	0.05	12
Co I	-0.08	0.04	5	-0.08	...	1
Ni I	0.04	0.06	24	0.03	0.07	6
Ce II	-0.23	0.04	4	-0.26	0.02	3
Nd II	-0.35	0.04	2	-0.15	...	1
Yb II	-0.01	...	1

^aC abundance: optical from CH, C₂, infrared from CO

^bN abundance: optical and infrared from CN

^cO abundance: optical from [O I], infrared from OH

^dlog ϵ values are given for Fe I and Fe II

Table 6. HIP 114809 Mean Abundances

Species	[X/Fe]	σ	#	[X/Fe]	σ	#
		optical			infrared	
C ^a	-0.35	0.04	...	-0.26	0.02	...
N ^b	0.57	0.58	0.02	...
O ^c	0.11	0.04	2	0.15	0.04	...
Na I	0.34	0.03	4	0.36	0.05	4
Mg I	0.16	0.04	2	0.14	0.04	11
Al I	0.10	0.05	4	0.20	0.09	6
Si I	0.22	0.08	14	0.23	0.04	11
P I	-0.03	...	2
S I	0.10	...	1	0.08	0.04	10
K I	0.75	...	1	0.11	0.02	2
Ca I	0.17	0.06	11	0.15	0.03	11
Sc I
Sc II	0.19	0.07	6
Ti I	0.01	0.08	9	0.07	0.03	7
Ti II	0.16	0.07	5	0.00	...	1
Cr I	0.04	0.08	11	0.03	0.04	3
Cr II	0.17	0.10	5
Fe I ^d	7.17	0.06	64	7.18	0.04	24
Fe II ^d	7.12	0.05	12
Co I	-0.05	0.03	5	-0.05	...	1
Ni I	0.10	0.07	23	0.12	0.06	6
Ce II	0.01	0.02	3	0.09	0.09	5
Nd II	0.08	0.06	2	1
Yb II	0.07	...	1

^aC abundance: optical from CH, C₂, infrared from CO

^bN abundance: optical and infrared from CN

^cO abundance: optical from [O I], infrared from OH

^dlog ϵ values are given for Fe I and Fe II

Table 7. $\log \epsilon(C)$ Values From Individual Features

Star	CH ^a G-band (Å)	C ₂ ^a Swan (Å)	C I 5052 (Å)	C I 5380 (Å)	C I 8335 (Å)	C I 16022 (Å)	C I 16890 (Å)	C I 17456 (Å)	C I 21023 (Å)	CO 23400 (Å)	CO 23700 (Å)
HIP 54048	7.64	7.65	7.70	7.77	7.82	7.73	7.83	7.83	7.73	7.73	7.73
HIP 57748	7.98	8.06	8.12	8.18	8.35	8.14	8.28	8.24	8.16	8.16	8.12
HIP 114809	7.72	7.78	7.75	7.91	7.91	7.86	7.94	7.94	7.84	7.85	7.82

^aG-band refers to the band heads in the 4300-4330 Å region. Swan refers to the band heads near 5160 and 5631 Å.

Table 8. Mean $\log \epsilon(\text{C})$ Values of Species and Final Derived Elemental Abundance

Star	CH	C ₂	C I _(opt)	C I _(IR)	CO	$\langle \log \epsilon(\text{C}) \rangle$	σ
HIP 54048	7.64	7.65	7.76	7.78	7.73	7.71	0.06
HIP 57748	7.98	8.06	8.22	8.21	8.14	8.12	0.10
HIP 114809	7.72	7.78	7.86	7.90	7.84	7.82	0.07

Table 9. Fe Abundances From Common Fe I Lines Used in Both SYN and EW Methods for HIP 114809.

Species	λ	χ	$\log gf$	$\log \epsilon(\text{Fe})_{\text{SYN}}$	$\log \epsilon(\text{Fe})_{\text{EW}}$	$\Delta_{(\text{SYN}-\text{EW})}$
Fe I	15194.49	2.22	-4.75	7.09	7.18	-0.09
Fe I	15207.53	5.39	0.08	7.24	7.22	0.02
Fe I	15343.79	5.65	-0.69	7.14	7.18	-0.04
Fe I	15493.52	6.36	-1.06	7.19	7.17	0.02
Fe I	15648.51	5.43	-0.70	7.14	7.17	-0.03
Fe I	15662.01	5.83	0.07	7.17	7.26	-0.09
Fe I	15761.31	6.25	-0.16	7.17	7.26	-0.09
Fe I	15858.66	5.58	-1.25	7.14	7.21	-0.07
Fe I	15980.73	6.26	0.72	7.19	7.27	-0.08
Fe I	16009.61	5.43	-0.55	7.18	7.27	-0.09
Fe I	16165.03	6.32	0.75	7.24	7.21	0.03
Fe I	16171.93	6.38	-0.51	7.22	7.25	-0.03
Fe I	17420.83	3.88	-3.52	7.24	7.24	0.00
Fe I	21178.16	3.02	-4.24	7.14	7.24	-0.10
Fe I	21238.47	4.96	-1.37	7.14	7.15	-0.01
Fe I	21284.35	3.07	-4.51	7.14	7.16	-0.02
Fe I	21735.46	6.18	-0.73	7.21	7.23	-0.02
Fe I	22257.11	5.06	-0.82	7.24	7.25	-0.01
Fe I	22260.18	5.09	-0.98	7.17	7.19	-0.02
Fe I	22419.98	6.22	-0.30	7.19	7.23	-0.04
Fe I	22473.26	6.12	0.32	7.22	7.16	0.06
Fe I	22619.84	4.99	-0.51	7.17	7.23	-0.06
Fe I	23308.48	4.08	-2.73	7.17	7.25	-0.08

SYN = spectrum synthesis, EW = equivalent width matching.

Table 10. $^{12}\text{C}/^{13}\text{C}$ Ratios
of Program Stars From Op-
tical and *IR* Regions

Stars	^{13}CN (8004 Å)	^{13}CO (2–0) (23440 Å)	^{13}CO (3–1) (23730 Å)
HIP 54048	10	12	12
HIP 57748	6	8	9
HIP 114809	...	15	16